

Lawrence Berkeley National Laboratory

LBL Publications

Title

Distributed fiber optic strain sensing of bending deformation of a well mockup in the laboratory

Permalink

<https://escholarship.org/uc/item/7h88500n>

Authors

Sasaki, Tsubasa

Zhang, Shenghan

Soga, Kenichi

et al.

Publication Date

2021-12-01

DOI

10.1016/j.jngse.2021.104309

Peer reviewed

26 which could improve the quality of distributed strain measurements with BOTDR/A. Results show that
27 the tight-buffered cable is best suited for strain sensing as its maximum errors in the strain measurement
28 were -36% and -24% against conventional sensors at the maximum elastic and plastic bending loads,
29 respectively, whereas those of the non-tight-buffered cable were -45% and -71%, respectively. Similar
30 trends were obtained in the bending curvature measurement. The detailed design of the tight-buffered
31 cable is presented to elucidate key characteristics of such a cable, which will facilitate accurate distributed
32 strain sensing in oil and gas wells.

33

34 Keywords

35 Distributed fiber optic sensing; distributed strain sensing; well integrity; well failure; fiber optic cable;
36 real-time monitoring

37

38 **1 Introduction**

39

40 Well integrity is a critical factor in subsurface energy exploration and management, not only in a
41 catastrophic event such as the Deepwater Horizon oil spill (McNutt, Camilli, et al. 2012; McNutt, Chu, et
42 al. 2012; Hickman et al. 2012) but also in more subtle events such as gas leakage from CO₂ sequestration
43 wells (Gasda, Bachu, and Celia 2004; Dou et al. 2020). In fact, many well integrity challenges occur in
44 conventional oil and gas wells in compacting reservoirs, such as at the Wilmington field (Nagel 2001;
45 Mayuga and Allen 1969; Roberts 1953), the Ekofisk field (Nagel 2001; Yudovich, Chin, and Morgan
46 1988; Schwall and Denney 1994), and the Belridge field (Dale, Narahara, and Stevens 1996; Fredrich et
47 al. 2000). As such, well integrity is pertinent to global energy production and consumption;
48 approximately 50% of the global energy in 2014 was still provided from oil and natural gas and their
49 consumption had steadily been increasing from 1965 to 2014, especially in the highest energy consumer
50 countries such as China, USA, and Russia (Aydin 2014; 2015; Aydin, Jang, and Topal 2016).

51

52 Fields with greater reservoir compaction exhibit more issues associated with loss of well integrity.
53 Methane hydrate reservoirs, in particular, are at significant risk of compaction, as the reservoir layer
54 usually consists of unconsolidated, soft sediment and substantial depressurization of pore water is carried
55 out to produce methane gas from the reservoir (Yamamoto 2015; Yamamoto et al. 2014; Yoneda et al.
56 2015). Currently, a number of field tests have been carried out to examine the potential of methane
57 hydrate reservoirs to produce an economic volume of methane gas to warrant commercial production
58 (Chen et al. 2018; Klar et al. 2019; Yamamoto et al. 2017; Yamamoto 2015; Yamamoto and Dallimore
59 2008; Yamamoto et al. 2014). To ensure the long-term safety and viability of gas production, it is
60 imperative to carry out real-time monitoring of well integrity in order to prevent unexpected well failures.
61 This will contribute to improving not only the safety but also the environmental and management aspects
62 of natural gas production, which are within the scope of natural gas science and engineering.

63

64 Distributed strain sensing (DSS) by fiber optics is an innovative approach to address the need of well
65 integrity monitoring, as it is capable of measuring deformations of wells with high accuracy in real-time,
66 which cannot be achieved by traditional distributed acoustic sensing (DAS) or temperature sensing (DTS)
67 techniques. It has already been shown in a previous study (Sasaki et al. 2019) that Brillouin time domain
68 reflectometry/analysis (BOTDR/A) is effective in monitoring the axial tensile deformation of a well
69 mockup.

70

71 DSS by fiber optics has been implemented in boreholes for various purposes, including but not limited to
72 subsurface subsidence monitoring (Zhang et al. 2018), hydromechanical characterization of the reservoir
73 (Lei, Xue, and Hashimoto 2019; Sun et al. 2020; Y. Zhang et al. 2020; Sun et al. 2021), estimation of the
74 flow of CO₂ plume in geological carbon storage (Sun et al. 2018), hydraulic fracturing monitoring
75 (Krietsch et al. 2018), and monitoring of landslides (Kogure and Okuda 2018). Novel fiber optic cables
76 have been developed which utilize chemo-mechanical coupling to detect hydrocarbon leakage in the well

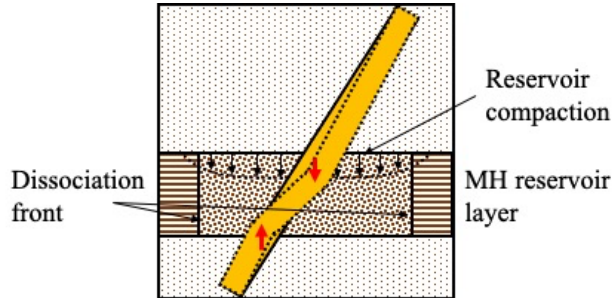
77 annulus (Wu 2019). Also, strain profiles in a fiber optic cable, which was embedded in a backfilled
78 borehole, are shown to match those in the surrounding formation (i.e., no cable slippage at cable-
79 formation interface) at moderate confining pressure levels, guaranteeing the quality of DSS data (Zhang
80 et al. 2018). However, fiber optic cables deployed in oil and gas wells are usually not in direct contact
81 with the formation, as the cables are typically cemented in the annulus behind the long casing string,
82 which casts doubt upon the applicability of their DSS results to deep subsurface wells. Also, the cables
83 employed in the above studies are not robust enough for in situ integrity monitoring of deep subsurface
84 wells in actual oil and gas fields. The pressures and temperatures encountered require the cable to be
85 engineered to resist the high collapse pressure and survive the elevated temperatures, while
86 simultaneously maintaining the sensitivity to the deformation of the formation.

87
88 In the previous study (Sasaki et al. 2019), various fiber optic cables were tested in an axially deformed
89 well mockup and evaluated for their robustness and strain sensitivity. It was found that the relevant
90 factors for increasing strain sensitivity, while maintaining the robustness for surviving in downhole
91 conditions, are tight-buffered coating layers around the optical fiber core and the number of coating layers
92 (i.e., the greater the tight-buffer is and the less the number of coating layers is, the better the strain
93 sensitivity).

94
95 A key challenge toward successful deployment of BOTDR/A in the field is the development of effective
96 DSS cables. Commercially available fiber optic cables for DAS and DTS are not suitable for DSS as
97 optical fibers in such cables are not tightly buffered to the outer cable sheath, which causes slippage of
98 fibers and undermines the accuracy of distributed strain measurements. In this study, new fiber optic
99 cables for DSS with BOTDR/A were developed and tested in a laboratory experiment. The fiber optic
100 cables were embedded in the annulus of a laboratory-scale well mockup, which consisted of outer and
101 inner steel pipes. The well mockup was then subjected to three-point bending to simulate bending
102 deformation of a deviated well during reservoir compaction. A schematic diagram depicting the bending

103 deformation of a deviated well during hypothetical compaction of a methane hydrate reservoir is provided
104 in Figure 1.

105



106

107

108 Figure 1 Bending well deformation in a methane hydrate reservoir [after Sasaki (2019)].

109

110 The primary objectives of this research are (i) to investigate the effectiveness of BOTDR/A to monitor
111 bending deformation of the well mockup, (ii) to assess the performance of different fiber optic cables in
112 monitoring strain and bending curvature development of the well mockup, and (iii) to identify key factors
113 in oil and gas cables affecting the accuracy of BOTDR/A measurements. The following sections of the
114 paper present details of the fiber optic cables and DSS techniques employed in this study, as well as
115 details of mockup preparation, load testing, and test results.

116

117 2 Methodology

118

119 2.1 Distributed fiber optic strain sensing interrogators

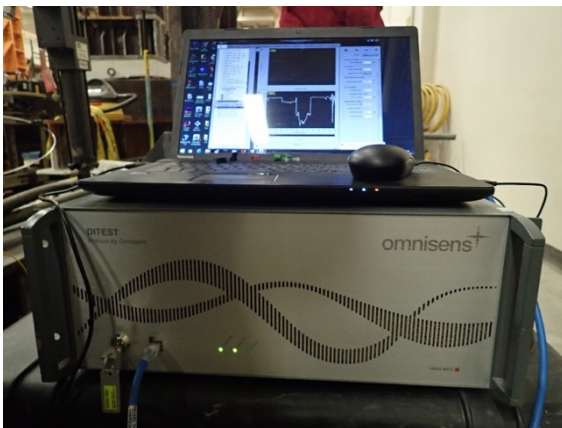
120

121 Two distributed fiber optic strain sensing interrogators were employed to obtain the strain profiles of the
122 well mockup; they are Omnisens Vision Dual interrogator and LUNA ODISI 6104 interrogator (Figure

123 2). Both interrogators utilize backscattering of incident light waves traveling in an optical fiber to infer
124 strain as well as temperature changes. The Omnisens measures the Brillouin backscattering spectra, which
125 is generated due to the interaction of incident light waves and carrier-deformation waves, via a
126 mechanism called Brillouin optical time domain reflectometry/analysis (BOTDR/A). The LUNA
127 measures the Rayleigh backscattering spectra, which is caused by random refractive index fluctuations in
128 an optical fiber, in the frequency domain via a mechanism called optical frequency domain reflectometry
129 (OFDR). The LUNA interrogator is analogous to Fiber Bragg Grating (FBG) interrogators in the sense
130 that OFDR utilizes an optical fiber as a long continuous array of weak FBGs with random periods.

131

132



133

134

(a)

(b)

135 Figure 2 Distributed fiber optic strain sensing interrogators: (a) Omnisens Vision Dual BOTDR/A; (b)

136

LUNA ODISI 6104.

137

138

139 The shifts in the Brillouin/Rayleigh backscattering spectra and strain/temperature changes are correlated
140 as shown in the following equations:

141

$$\Delta\nu_B = C_{\epsilon,B} \Delta\epsilon + C_{T,B} \Delta T \quad (1)$$

$$\Delta\nu_R = C_{\epsilon,R} \Delta\epsilon + C_{T,R} \Delta T \quad (2)$$

142 where $\Delta\nu_B$ is a frequency shift in the Brillouin backscattering spectra, $\Delta\nu_R$ is a frequency shift in the
 143 Rayleigh backscattering spectra, $C_{\epsilon,B}$ is the strain coefficient for Brillouin backscattering, $C_{T,B}$ is the
 144 temperature coefficient for Brillouin backscattering, $C_{\epsilon,R}$ is the strain coefficient for Rayleigh
 145 backscattering, $C_{T,R}$ is the temperature coefficient for Rayleigh backscattering, $\Delta\epsilon$ is a strain change, and
 146 ΔT is a temperature change. The values of the strain/temperature coefficients vary with interrogator and
 147 cable types. The coefficient values specific to the experimental settings of this study are provided in Table
 148 1. Details about the cable types are provided in the following section.

149
 150 Table 1 Strain and temperature coefficient values of the fiber optic cables.

Cable type	Interrogator type	Strain coefficient (MHz/%)	Temperature coefficient (MHz/°C)
Cable 1 (ver. 1)	Omnisens	300	1.0
Cable 1 (ver. 2)	Omnisens	500	1.0
Cable 2	Omnisens	500	1.0
Cable 3	LUNA	$1.50 \cdot 10^6$	$1.57 \cdot 10^3$

151
 152
 153 The LUNA interrogator is capable of measuring precise strain profiles with extremely dense datapoints
 154 and high spatial resolution, to the point where submillimeter crack detection is possible (Zhang, Liu,
 155 Coulibaly, et al. 2020; Zhang, Liu, Cheng, et al. 2020). It is for this reason that the LUNA interrogator is
 156 used as the reference strain measurement in this study. A disadvantage of the LUNA interrogator is the
 157 short measurement length of up to 50 m, which makes it unsuitable for field measurements. BOTDR/A,
 158 on the other hand, measures averaged strain profiles over its spatial resolution of roughly 1 m but can

159 measure tens of kilometers of strain/temperature profiles along a single fiber optic cable. Therefore,
 160 BOTDR/A is well suited to monitoring the mechanical/thermal behavior of infrastructure such as tunnels
 161 (Gue et al. 2015; Mohamad et al. 2012; 2010), bridges (Butler et al. 2016), pipelines (Inaudi and Glisic
 162 2006), piles (Klar et al. 2006; Pelecanos et al. 2017; 2018; Mohamad et al. 2011), and subsurface wells
 163 (Sun et al. 2020; 2021). Further details for civil infrastructure applications can be found in Kechavarzi et
 164 al. (2016) and Soga and Luo (2018). Measurement performance characteristics of each interrogator are
 165 provided in Table 2.

166

167 Table 2 Measurement performance of the fiber optic interrogators.

	Omnisens Vision Dual (BOTDA)	LUNA ODiSI 6104
Spatial resolution (cm)	75	-- **
Sampling interval (cm)	25	0.26 *
Precision (2σ) ($\mu\epsilon$)	± 4	± 6
Measurement distance (km)	60	0.050
Measurement rate (Hz)	N/A	10

168 * Sampling interval can range between 0.065 cm to 0.26 cm.

169 ** The gauge length (i.e., spatial resolution) is undefined but increases with increasing sampling
 170 interval.

171

172

173 2.2 Fiber optic cables for DSS measurement

174

175 Three different fiber optic cables were examined in this study: Cable 1 (tight-buffered FIMT), Cable 2
176 (loose FIMT), and Cable 3 (non-FIMT baseline). The cross-sections of these cables are provided in
177 Figure 3. The cross-section of the previous version of Cable 1, which was tested in a separate experiment
178 prior to the present experiment, is also provided in Figure 3, which is referred to as Cable 1 (version 1).
179 The primary difference between Cable 1 (ver. 1) and Cable 1 (ver. 2) is the axial separation between the
180 fiber-optic elements; Cable 1 (ver. 2) has a reduced axial separation than Cable 1 (ver. 1) so as to improve
181 strain transfer from the outer metal tube to the optical fibers. Details about the previous experiment are
182 omitted as they significantly overlap with those of the present experiment.

183

184 Cable 1 is tailored for integrated monitoring of oil and gas wells. It is equipped with a DSS FIMT (fiber
185 in metal tube) and a FIMT containing a DTS (distributed temperature sensing) fiber in a 1/4 in. OD metal
186 tube. The outer metal tube is filled with polymer. The advantages of the current version of Cable 1
187 relative to the previous version are that (i) the DSS FIMT is tightly buffered to the metal sheath with an
188 extra skim-coat polymer layer, (ii) the surface of the DTS FIMT is coated with a slip agent which
189 enhances slippage and hence the strain-independence of the DTS FIMT, and (iii) the DSS FIMT is
190 positioned closer to the center inside the cross-section of the metal sheath so as to improve strain transfer
191 from the metal sheath to the DSS FIMT.

192

193 Cable 2 has been designed for integrated fiber-optic monitoring of oil and gas wells. The FIMT contains
194 fibers for DAS (distributed acoustic sensing) and DTS. External to the FIMT is a tight buffered single-
195 mode optical fiber (without a metal tube) for DSS.

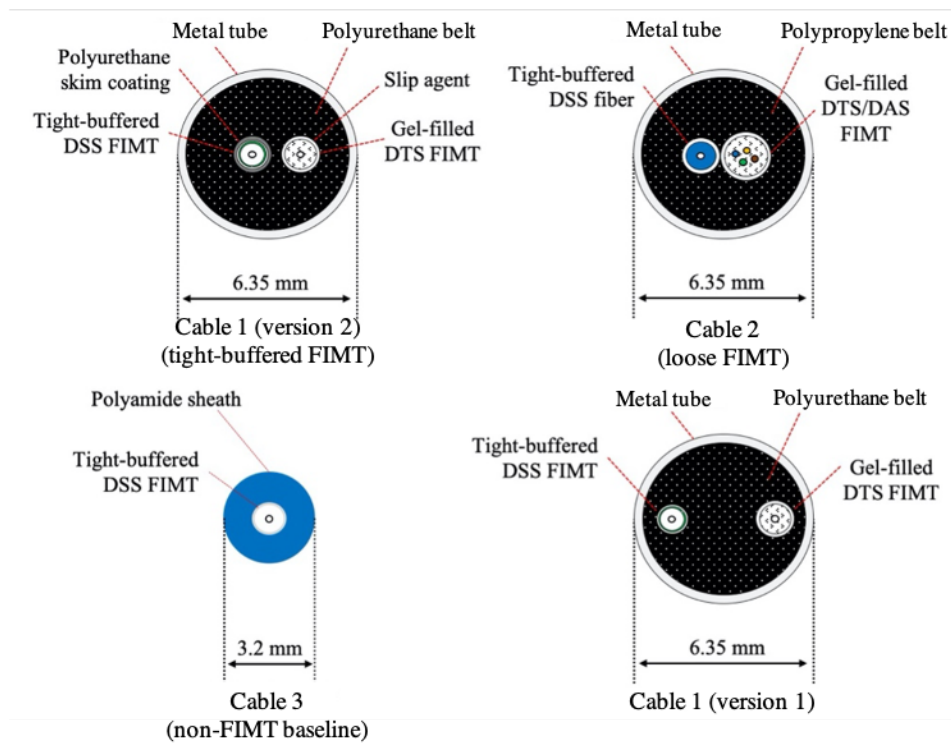
196

197 Cable 3 was used with the LUNA interrogator for the reference strain measurement. It is a commercially
198 available fiber optic cable that is often used in civil infrastructure monitoring (Cola et al. 2019; Rabaiotti
199 et al. 2017; Fabris et al. 2021; Zhang, Liu, Coulibaly, et al. 2020). Its design is much simpler than that of

200 Cable 1 and 2 as it is not designed to survive in harsh subsurface conditions where oil and gas wells are
201 usually constructed.

202
203 Distributed strain profiles along Cable 1 and 2 were measured with the Omnisens BOTDR/A interrogator,
204 whereas those along Cable 3 were measured with the LUNA interrogator.

205
206



207
208 Figure 3 The cross-sections of the fiber optic cables examined in this research. Cable 1 (version 2), 2, and
209 3 are tested in the present experiment, whereas Cable 1 (version 1) was tested in a previous experiment.

210

211 3 Well mockup preparation

212

213 3.1 Configuration

214

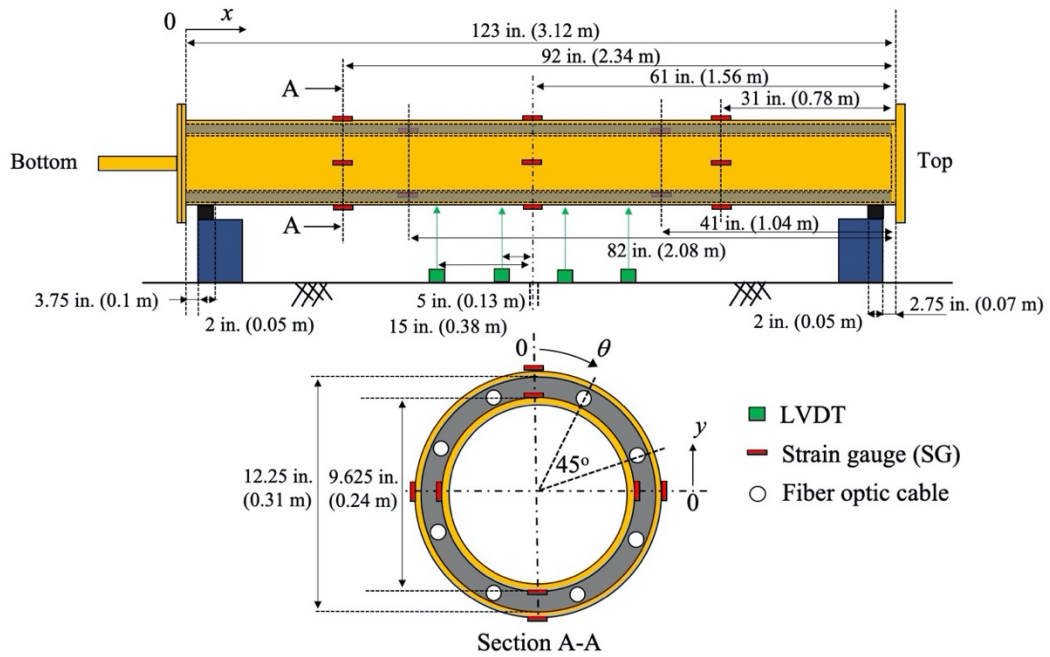
215 Figure 4 shows the cross-sections of the well mockup. It consists of a 9 5/8 in. (0.24 m) OD (outer
216 diameter) inner pipe and a 12 1/4 in. (0.31 m) ID (inner diameter) outer pipe with a wall thickness of 3/8
217 in. (9.53 mm) and 1/4 in. (6.35 mm), respectively. The inner pipe is assumed to be the casing and the
218 deformation of the outer pipe mimics the strain transferred from the formation into the cement sheath., as
219 the diameters of the pipes correspond to the diameter of casing and borehole of monitoring wells at the
220 Nankai Trough (Yamamoto et al. 2014). The length of the mockup is 123 in. (3.12 m), which is roughly
221 four times the spatial resolution of the Omnisens interrogator using the BOTDA mode. The support stand
222 at the bottom of the concentric assembly is a spacer which creates a gap between the ground and the
223 assembly. When it is positioned vertically to facilitate cementing, the gap protects the fiber optic cables
224 from mechanical damage. As such, the support stand does not take any bending moment or shear stress
225 and it has no effect on the bending behavior of the mockup.

226

227 At the beginning of mockup preparation, the pipes were separated as shown in Figure 5a. The inner pipe
228 was inserted into the outer pipe after the fiber optic cables had been installed in the annulus to assemble
229 the well mockup. There are eight cable sections in the mockup annulus as shown in Section A-A (Figure
230 4), which are created by aligning the holes on the top, bottom, and middle (gusset) plates (Figure 5b).
231 These aligned holes ensured that the fiber optic cables were positioned parallel to the axis of the mockup
232 and separated by a 45° angle from one another in the circumferential direction.

233

234



235

236

Figure 4 A cross-sectional schematic of the well mockup.



237

238

(a)

(b)

239

Figure 5 The well mockup before assembling: (a) inner and outer pipes; (b) gusset plates at the middle

240

length of the inner pipe that are attached for fiber optic cable installation.

241

242 3.2 Sensor installation

243

244 The well mockup was instrumented with strain gauges and LVDTs (linear variable differential
245 transformers) to compare to fiber optic measurements. The locations of the sensors are shown in Figure 4.

246 The strain gauges were attached on the surface of the inner and outer pipes at four circumferential
247 locations, which were offset 90° from one another, and at two (inner pipe) and three (outer pipe)

248 longitudinal locations, respectively. The LVDTs were installed on the lower surface of the outer pipe at
249 four longitudinal locations.

250

251 Figure 6 shows the locations of the fiber optic cables in the annulus of the well mockup. The fiber optic
252 cables were installed prior to mockup assembling by passing through the cables along each annular

253 segment (#1-#8). The cables were run through three longitudinally aligned holes in each segment (one
254 hole each on the top, bottom, and middle gusset plates). In order to measure bending deformation, the

255 cables of the same type were positioned diagonally across the circumferential cross-section of the

256 mockup. For instance, Cable 1 was installed in the segment 1 and 5, Cable 2 in the segment 3 and 7, and

257 Cable 3 in the segment 2, 4, 6, 8.

258

259 Cable 1 and 2 were spliced at the bottom exit of segment 3, 5 and 7 to form a closed loop which is a

260 prerequisite for performing Omnisens measurements in the BOTDA mode. Cable 3 was terminated at the

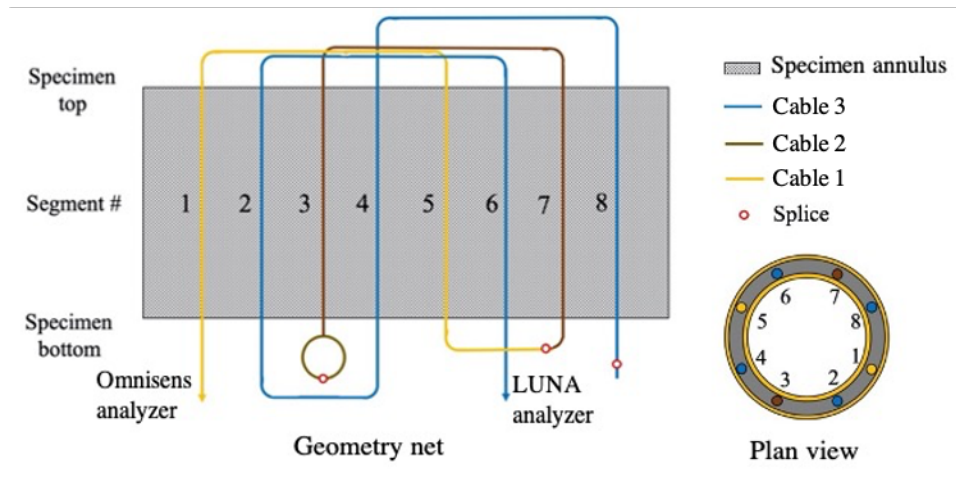
261 bottom exit of segment 8 to eliminate back reflection of the input light so as to increase the precision of

262 LUNA measurements.

263

264

265



266

267

Figure 6 The positions of the fiber optic cables in the mockup annulus.

268

269 3.3 Annulus cementing

270

271 After the fiber optic cable installation, the mockup was set up vertically and fixed against a steel column

272 so that cementing could be carried out. Cement slurry was prepared by mixing Portland cement with

273 water at a 0.44 water-to-cement ratio. A 0.75% by volume shrinkage reducing admixture was added to the

274 slurry while it was mixed. Slurry was mixed in four separate batches by a handheld drill at a rotation

275 speed of about 1,000 rpm (rotation per minute) for 10 min before each batch was poured into the mockup

276 annulus. The cement was cured under room temperature and humidity conditions for five days prior to the

277 bending test.

278

279 **4 Bending loading experiment**

280

281 4.1 Loading scheme

282

283 After five days of cement cure, the mockup was set up in the loading frame (Figure 7). Bending loading

284 was applied by pulling the fixture attached at the middle of the mockup downward. This was

285 accomplished by connecting the fixture with a rod that passes through a hole in the floor down to the

286 basement ceiling where the rod couples to an actuator and a load cell.

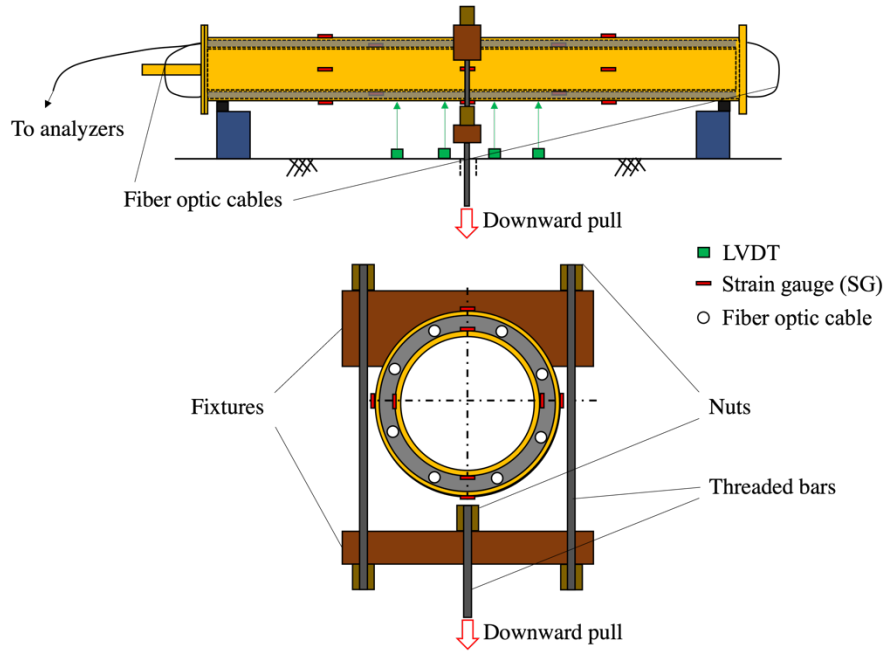
287



288

289

(a)



(b)

290

291

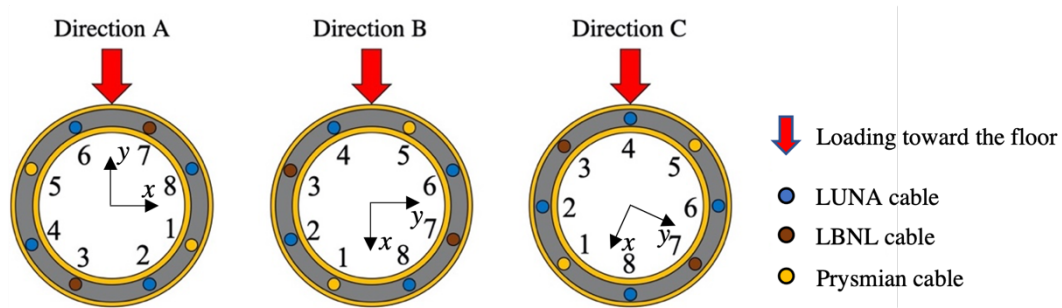
292 Figure 7 The mockup setup for the bending loading experiment: (a) an overview; (b) a schematic of cross-
 293 sections of the mockup.

294

295 The mockup was tested in three-point bending in three different directions as shown in Figure 8. The
 296 direction A was the initial configuration, whereas the direction B and C were subsequently set up by

297 rotating the mockup 90 and 112.5 degrees clockwise from the initial configuration, respectively. The
 298 direction A is intended for the evaluation of the performance of Cable 2 against the LUNA measurement,
 299 whereas the direction B tests Cable 1 against the LUNA measurement. In the direction A, Cable 2 is
 300 positioned further away from the neutral plane ($y = 0$) (segment #3 and #7) than Cable 1 (segment #1 and
 301 #5), which provides Cable 2 with a greater sensitivity to capture bending deformation. Thus, the direction
 302 A is suited to the performance evaluation of Cable 2. The same logic applies to the direction B, which is
 303 optimized for the evaluation of Cable 1 performance. The direction C is intended for the direct
 304 comparison of the performance of Cable 1 and 2, as the distance from the neutral plane to the cable
 305 segments was identical for both cables in this loading configuration.

306
 307



308
 309

310 Figure 8 Loading directions with regard to the positions of the cable segments.

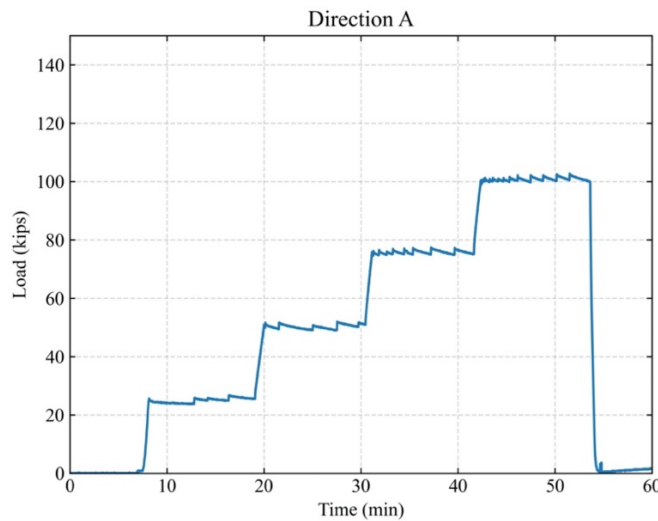
311

312 The loading was carried out sequentially in direction A, B, and C. Figure 9 shows the time series of
 313 bending loading in direction A. The load was increased by discrete increments in a stepwise manner. Each
 314 load increment was held for roughly ten to fifteen minutes so that fiber optic readings could be obtained
 315 from both Omnisens and LUNA interrogators. The Omnisens BOTDA performed a single measurement
 316 per load increment (~10 min), whereas the LUNA interrogator was taking ten readings per second (i.e.,
 317 dynamic measurement at 10 Hz). Accumulated LUNA readings were averaged to produce one

318 measurement per load increment to facilitate performance comparison with the Omnisens interrogator. It
319 is noted that the room temperature did not change by more than $\pm 0.3^{\circ}\text{C}$ during the entire testing period,
320 which was measured by a handheld non-contact infrared thermometer. Hence, the effect of temperature
321 change on fiber optic measurement results (Equation 1 and 2) is negligible.

322

323



324

325 Figure 9 Loading time series for the direction A case.

326

327 Once the load level reached a specified limit, the mockup was unloaded and then rotated to change the
328 loading direction. Another loading with stepwise increments was then resumed. The loading was kept in
329 the elastic range of the mockup (< 100 kips (kilopounds) ($1 \text{ kips} = 4.448 \text{ kN}$)) for the direction A and B
330 cases, whereas it was increased into the plastic range (> 100 kips) for the direction C case. Therefore,
331 measurements in the direction A and B cases provided the cable performance for capturing elastic
332 bending deformation of the well, while those in the direction C case provided that for measuring plastic
333 bending deformation of the well.

334

335

336 4.2 BOTDA and OFDR measurement results

337

338 4.2.1 Direction A

339

340 Figure 10 shows strain changes along the mockup measured by the Omnisens BOTDA (Figure 10a) and
341 the reference LUNA OFDR (Figure 10b) in the direction A case. Both figures show a triangular strain
342 distribution at each load increment with the maximum (largest tension) and minimum (largest
343 compression) strain magnitudes occurring at the middle of the mockup (i.e., 1.5 m) as expected in beam
344 deformation in three-point bending.

345

346 The comparison between the BOTDA and LUNA results reveals that Cable 2 measured the peak tensile
347 strain value of approximately 1,800 $\mu\epsilon$, whereas LUNA measured 2,400 $\mu\epsilon$, at the load level of 100 kips.
348 It is noted that LUNA can measure local, submillimeter-scale strain profiles, whereas BOTDA measures
349 averaged strain profiles over its spatial resolution (i.e., 0.75 m). By taking that into account, the difference
350 in the maximum tensile strain levels measured by BOTDA (with Cable 2) and LUNA (with Cable 3)
351 indicates good agreement between the two cables. The same is also true for the maximum compressive
352 strain levels (i.e., segment 6 (Cable 3) vs. 7 (Cable 2)).

353

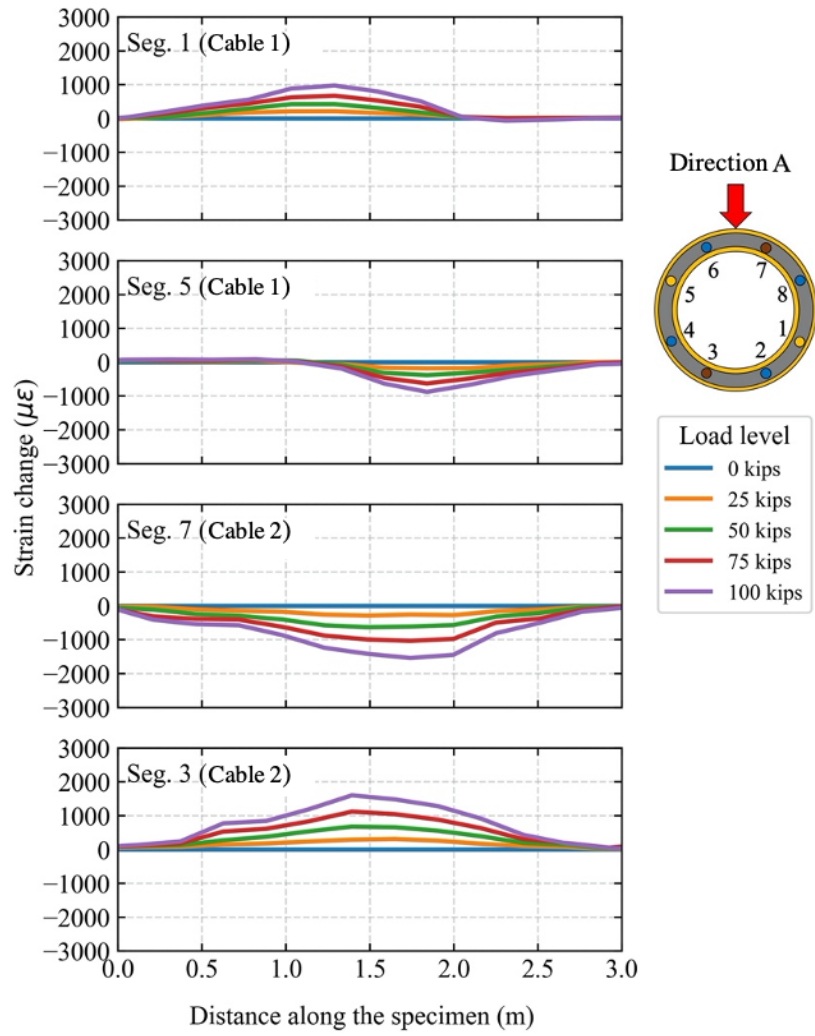
354 The above trends are also evident in the stress-strain curves at the center of the mockup (Figure 10c), as
355 the BOTDA and LUNA stress-strain profiles are in good agreement with the latter consistently showing
356 larger strain magnitudes at each stress level than the former. Note that the stress was calculated from the
357 Bernoulli-Euler beam theory (i.e. $\sigma = (M/I)y$, where σ is the longitudinal stress, M is the bending moment,
358 I is the second moment of area, and y is the distance from the neutral plane), so it represents an average
359 theoretical bending stress in the composite steel-cement cross-section of the well mockup.

360

361 Due to the spatial averaging nature of the BOTDA measurement, the strain distributions in Figure 10a are
362 smooth. In contrast, significant fluctuations are observed in the LUNA measurements on the tensile side
363 (i.e., segment 2 and 4 in Figure 10b). As the fluctuations occur only on the tensile side, it is not solely due
364 to the local nature of the LUNA measurement. The main cause is plastic deformation of the cement
365 (where the fiber optic cables are embedded). The cement deformed plastically on the tensile side of the
366 mockup creating miniature cracks (i.e., the upper half of the mockup cross section), whereas the
367 compressive side (i.e., the lower half) remained largely intact as the tensile strength of cement is about
368 one tenth of its compressive strength (Teodoriu et al. 2012).

369

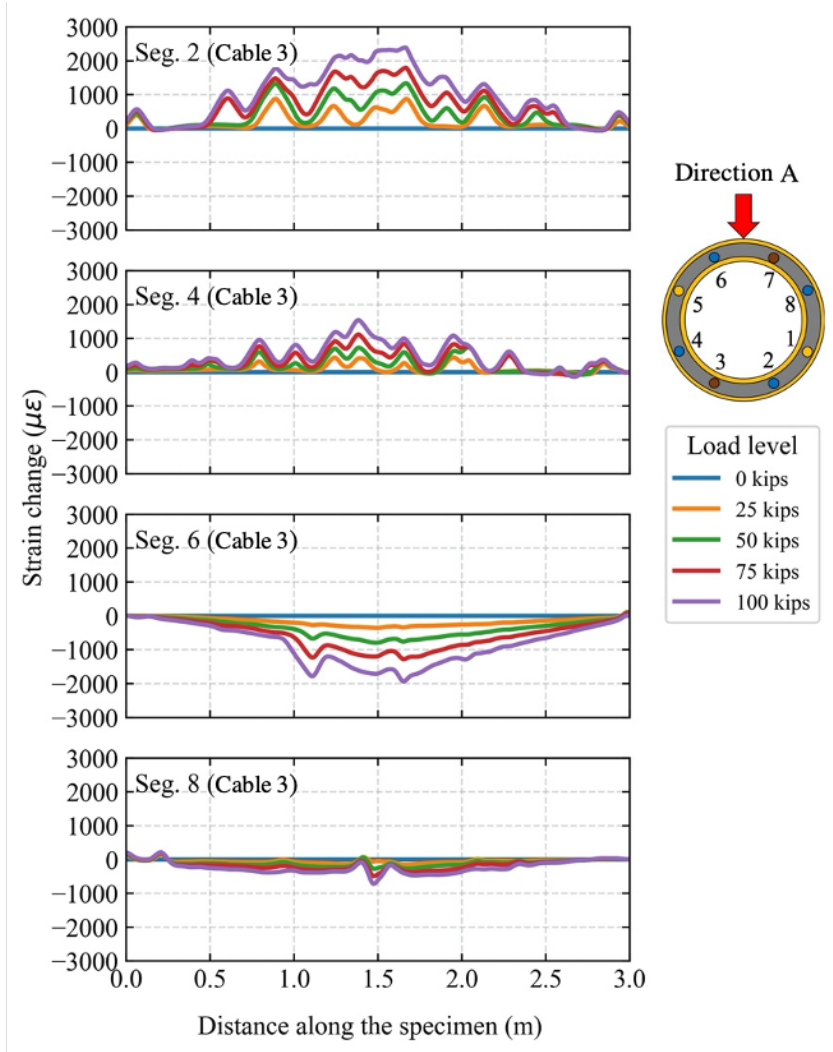
370



371

372

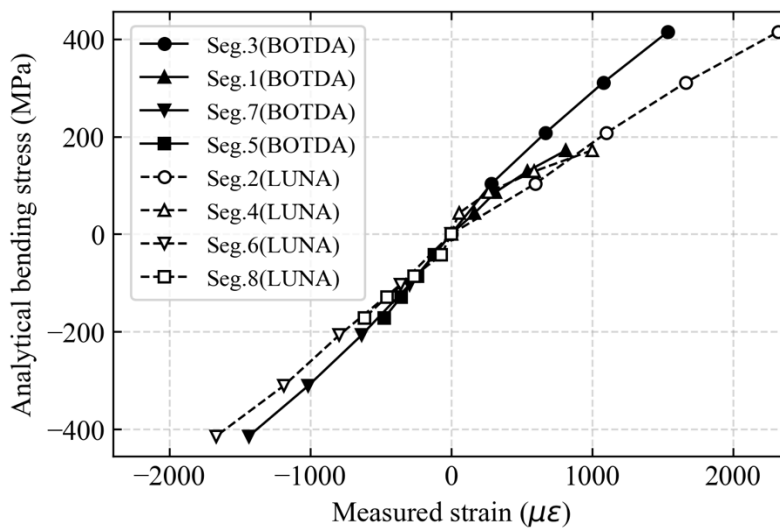
(a)



373

374

(b)



375

376
377
378
379
380
381
382
383
384
385
386
387
388
389
390
391
392
393
394
395
396
397
398
399

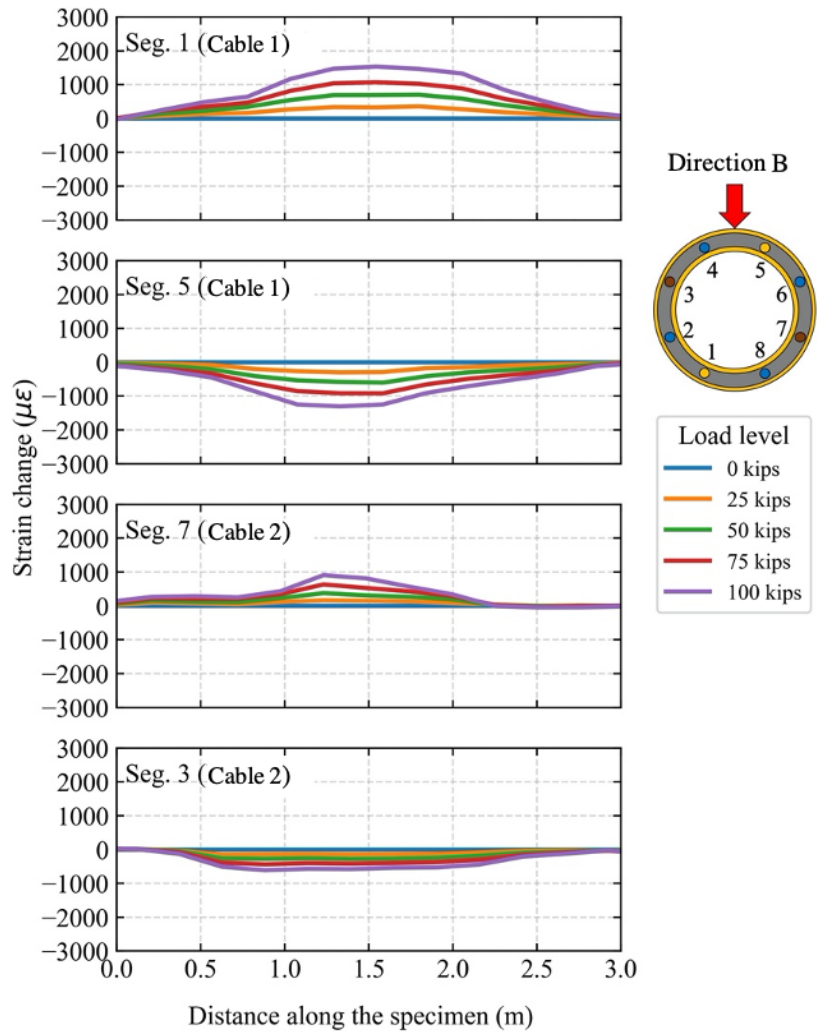
(c)

Figure 10 Strain changes in the mockup during loading in the direction A: (a) Omnisens BOTDA readings along Cable 1 and 2; (b) reference LUNA OFDR readings along Cable 3; (c) analytical bending stress vs. measured strain at the center of the mockup.

4.2.2 Direction B

Figure 11 shows the strain development in the mockup during loading in the direction B case. It is observed that the maximum and minimum strain magnitudes at 100 kips for Cable 1 are approximately 1,800 $\mu\epsilon$ and -1,300 $\mu\epsilon$, respectively, whereas those for the reference Cable 3 are 2,700 $\mu\epsilon$ and -1,700 $\mu\epsilon$. The differences between Cable 1 and 3 results seem significant but if the strain values near the maximum and minimum values in the LUNA readings (Cable 3) are averaged over the spatial resolution of the Omnisens BOTDA (i.e., 0.75 m), these values decrease to approximately 2,000 $\mu\epsilon$ and 1,500 $\mu\epsilon$. Therefore, the LUNA readings are in good agreement with the values measured for Cable 1. That is, the strain sensing performance of Cable 1 is validated against the reference LUNA result.

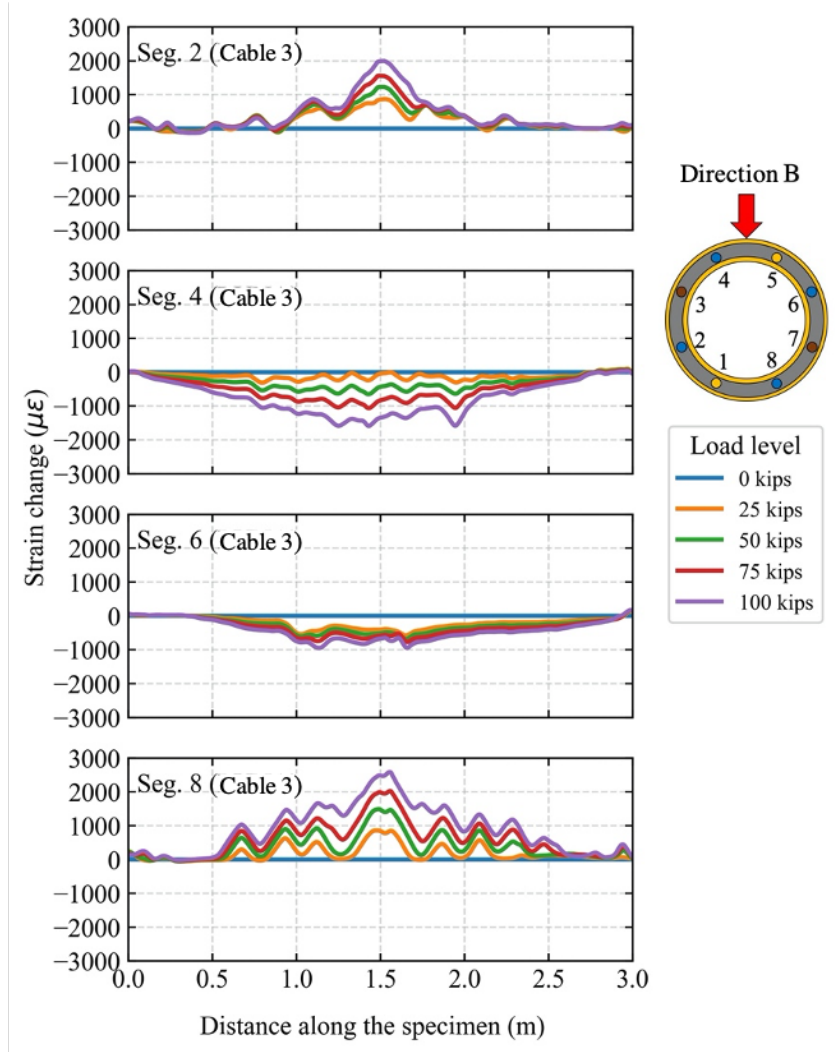
Although it is not directly related to the cable performance, it is noteworthy that the tensile deformation in the cement during loading in the direction A case has been plastic (i.e., irreversible). This is suspected because strain fluctuations in the LUNA results are observed not only on the tensile side (i.e., segment 1, 2, 7, 8) but also on the compressive side at the segment 4, which was on the tensile side in the direction A case. Hence, the portions of the cement that were subjected to tensile deformation beforehand might no longer be elastic even though the mockup as a whole still behaved predominantly elastically against bending.



400

401

(a)



402

403

(b)

404 Figure 11 Strain changes in the mockup during loading in the direction B: (a) Omnisens BOTDA readings

405

along Cable 1 and 2; (b) reference LUNA OFDR readings along Cable 3.

406

407 4.2.3 Direction C

408

409 Figure 12 shows the strain distributions during loading in the direction C case. Under direction A and B

410

loading, the strain values for Cable 1 and 2 were noted to be comparable to those for the reference Cable

411

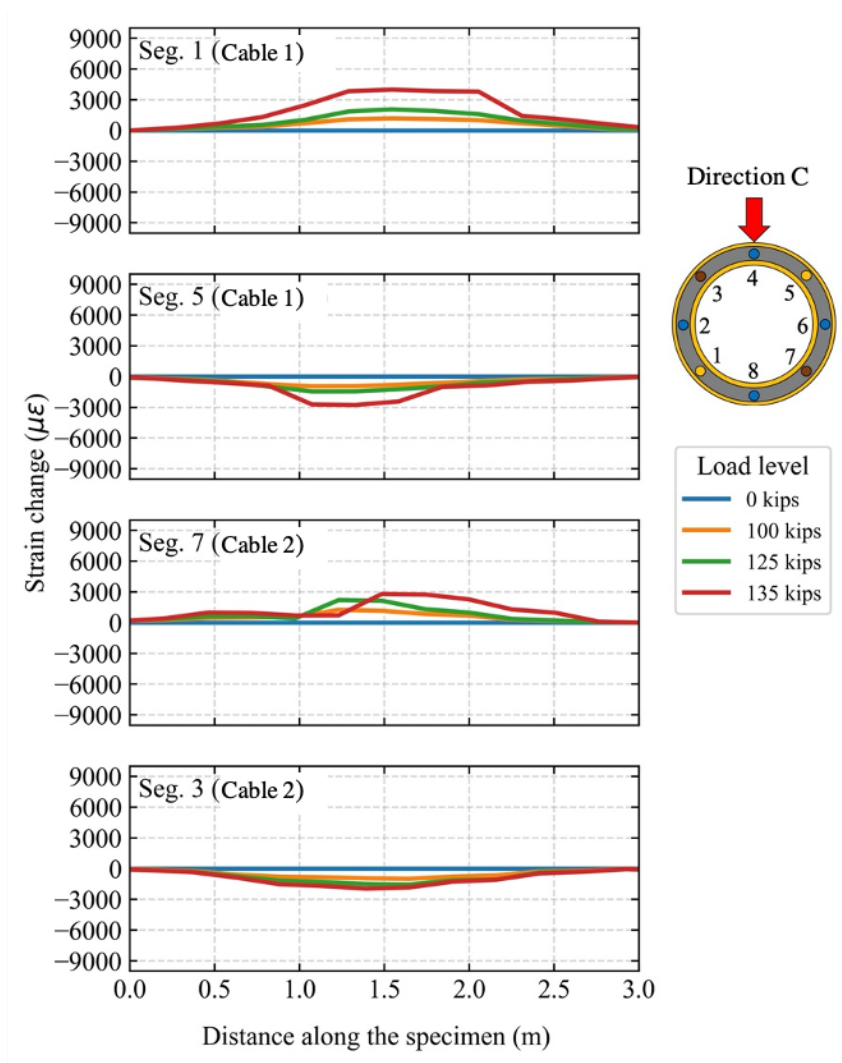
3, and hence the strain sensing performance of Cable 1 and 2 was validated. However, the strain sensing

412 performance in the plastic range (i.e., loading in the direction C) varied significantly between the two
413 cables. It is noted that the loading was terminated at 135 kips where the mockup accumulated bending
414 deflection without an increase in bending load.

415
416 Figure 12a shows that the peak strain values at 135 kips for Cable 1 are larger than that for Cable 2. The
417 maximum and minimum values are approximately 4,000 $\mu\epsilon$ and -3,000 $\mu\epsilon$ for Cable 1, whereas those are
418 3,000 $\mu\epsilon$ and -2,000 $\mu\epsilon$ for Cable 2. Also, the peak strain changes between 125 kips and 135 kips are
419 much smaller for Cable 2 than for Cable 1. Of particular interest is the strain level decrease (instead of an
420 increase) between 125 kips and 135 kips for Cable 2 between 1.0 m and 1.5 m in the segment 7, which
421 suggests slippage of the DSS fiber in Cable 2. Signs of DSS fiber slippage are not observed in Cable 1.
422 The superior strain sensing performance of Cable 1 could be attributed to better attachment of its DSS
423 FIMT to the surrounding polymer filling by means of pressure and/or adhesion. The DSS fiber in Cable 2
424 is not encased in a metal tube (instead it is covered in a second polymer coating), which might have
425 hindered adhesion of the DSS fiber to the surrounding polymer layer that fills the space inside the metal
426 tube.

427
428 The LUNA readings (Cable 3) cannot be compared directly with those the BOTDA readings for Cable 1
429 and 2 in the direction C case, as the distance from the neutral plane to Cable 3 was different than the
430 distance to Cable 1 and 2. Larger strain magnitudes are expected for cables positioned further from the
431 neutral plane (Cable 3 in segment 4 and 8) than those nearer to the neutral plane (Cable 1 and 2 in the
432 segment 1, 3, 5, and 7). As expected, the peak strain magnitudes at 135 kips were significantly larger in
433 Cable 3: approximately 7,000 $\mu\epsilon$ in segment 8 and -6,000 $\mu\epsilon$ in segment 4. If an average is taken over the
434 spatial resolution of the Omnisens BOTDA (0.75 m), the peak values would decrease to roughly 5,000 $\mu\epsilon$
435 and -4,000 $\mu\epsilon$, respectively. These values have to be multiplied by the ratio of distances from the neutral
436 plane to facilitate a comparison with the peak values for Cable 1 and 2. The ratio is

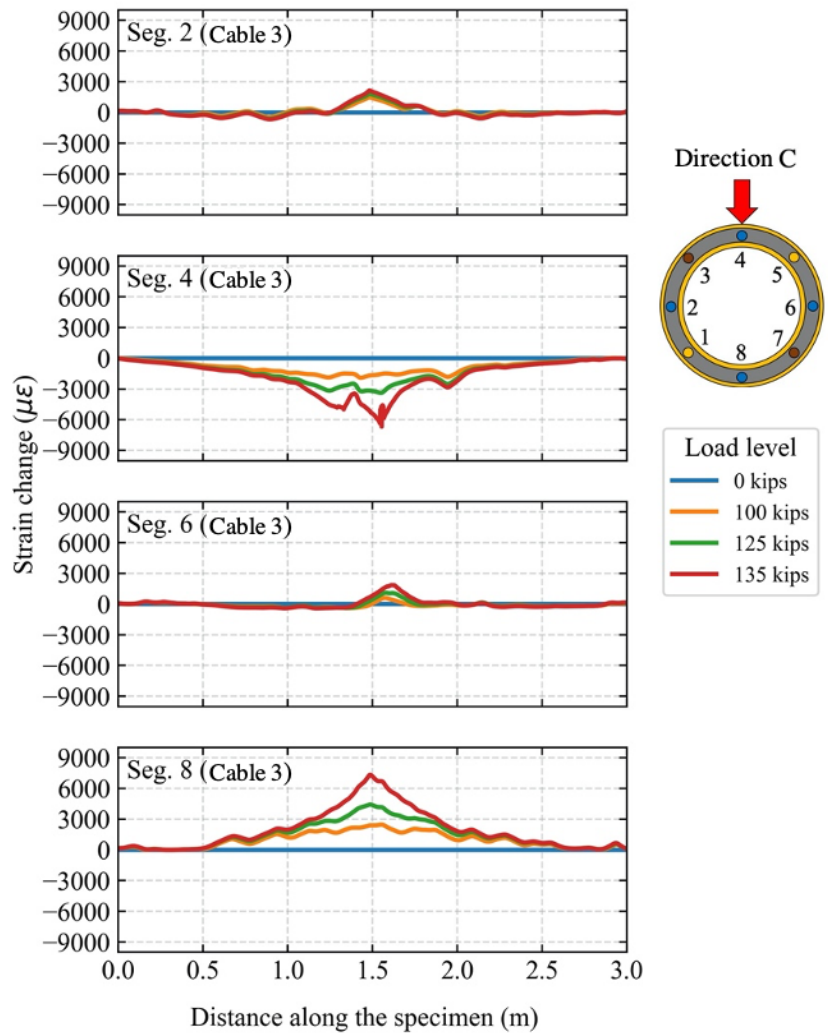
437 $\sin 45^\circ / \sin 90^\circ = 0.71$. Therefore, the corrected strain values for Cable 3 would be roughly 3,600 $\mu\epsilon$ and
 438 -2,800 $\mu\epsilon$, respectively. These values are in good agreement with those obtained in Cable 1 (4,000 $\mu\epsilon$ and
 439 -3,000 $\mu\epsilon$), but slightly underestimated in Cable 2 (3,000 $\mu\epsilon$ and -2,000 $\mu\epsilon$). This comparison reveals that
 440 Cable 1 demonstrates a better strain sensing performance than Cable 2 in the plastic bending deformation
 441 range of the mockup.
 442



443

444

(a)



445

446

(b)

447 Figure 12 Strain changes in the mockup during loading in the direction C: (a) Omnisens BOTDA readings

448

along Cable 1 and 2; (b) reference LUNA OFDR readings along Cable 3.

449

450 4.2.4 Temperature change

451

452 Although the evaluation of the strain sensing performance of fiber optic cables is the main focus of this

453

study, the assessment of temperature sensing performance is also important, not only for DTS

454

measurements with BOTDR/A but also for the temperature compensation of strain readings (Gue et al.

455 2015; Mohamad, Soga, and Amatya 2014; Pelecanos et al. 2018). Of particular importance is the isolation
456 of temperature fibers from strains. BOTDR/A estimates temperature changes from the thermal
457 expansion/contraction of DTS fibers, which are only several tens of microstrains per degree Celsius.
458 Slight mechanical strains applied to the DTS fibers quickly distort the temperature measurement.

459

460 Strain isolation performance of the DTS fibers in Cable 1 and 2 are evaluated, in order to identify a key
461 factor for achieving a better strain isolation of DTS fibers. Figure 13 shows temperature changes
462 measured by the Omnisens BOTDA for Cable 1 and 2 during loading in the direction A case. The
463 temperature changes are fictitious because the room temperature in the laboratory did not fluctuate by
464 more than $\pm 0.3^{\circ}\text{C}$ from 25°C throughout the entire testing period, which was validated by infrared
465 thermometer readings.

466

467 The erroneous temperature changes are caused by strain development in the DTS fibers in Cable 1 and 2.
468 It is found that Cable 2 shows a significantly better strain isolation performance than Cable 1, as the
469 magnitudes of the fictitious temperature changes are much smaller in Cable 2 than Cable 1 (e.g., roughly
470 $\pm 10^{\circ}\text{C}$ (Cable 1) vs. $\pm 3^{\circ}\text{C}$ (Cable 2) at 100 kips) despite Cable 2 positioned further from the neutral
471 plane.

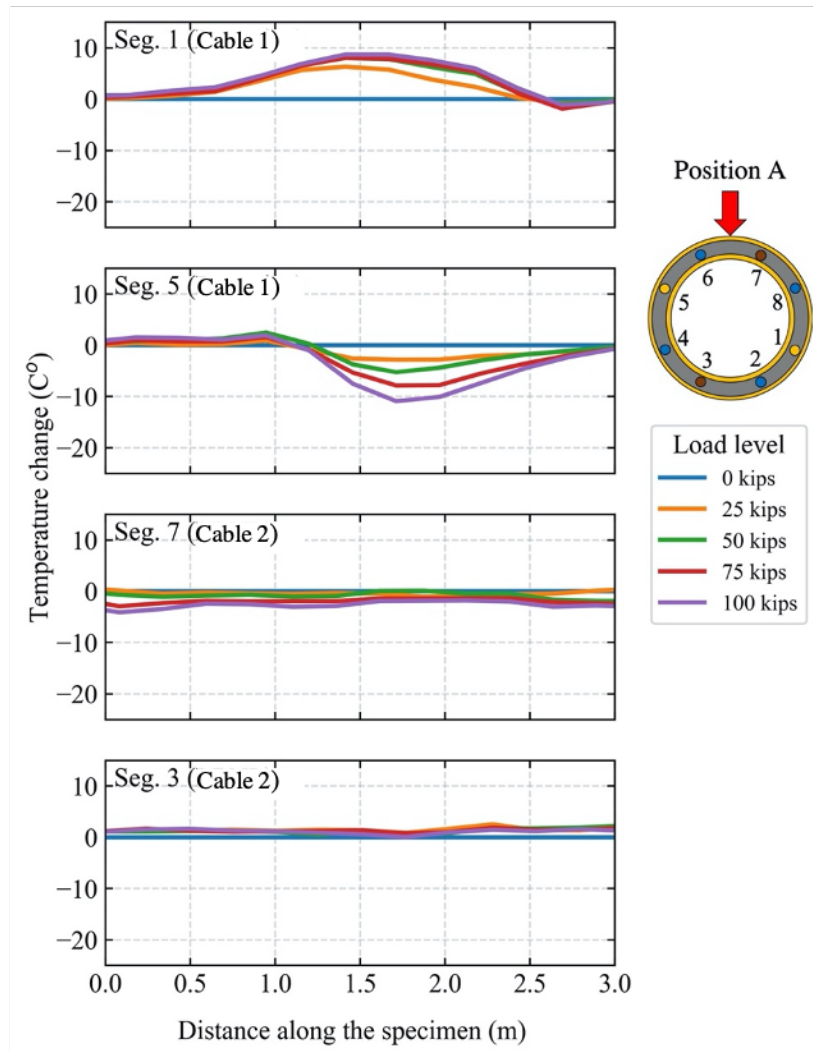
472

473 The difference in the strain isolation performance of Cable 1 and 2 is attributed to the difference in the
474 diameter of DTS FIMT: 1.8 mm OD for Cable 2 vs. 1.35 mm OD for Cable 1. The larger diameter DTS
475 FIMT might have been able to accommodate strains without stretching/compressing the fibers encased in
476 it. Also, the difference in stiffness of the belt material might have played a role (i.e., polyurethane (Cable
477 1) is softer than polypropylene (Cable 2)). It is noted that the DTS FIMTs in both Cable 1 and 2 were
478 filled with gel so whether the FIMT was gel-filled or not is not a factor affecting the strain isolation

479 performance herein. Also, the abovementioned trends of the fictitious temperature changes are found
480 valid regardless of the loading direction (i.e., elastic or plastic loading range).

481

482



483

484 Figure 13 Fictitious temperature changes calculated from Omnisens BOTDA readings for Cable 1 and 2

485

during loading in the direction A.

486

487 5 Discussion

488

489 5.1 Bending curvature analysis

490

491 Curvature development of the mockup during loading is estimated from readings of the instrumented
492 sensors. Bending curvature values from the strain gauges (SGs) and fiber optics are calculated from the
493 following equation:

494

$$\kappa = (\epsilon_{lower} - \epsilon_{upper}) / (2y) \quad (3)$$

495

496 where κ is the bending curvature, y is the distance from the neutral plane (see Figure 4); ϵ_{lower} is a strain
497 value in the lower half of the mockup cross-section; ϵ_{upper} is a strain value in the upper half of the
498 mockup cross-section. It is noted that ϵ_{lower} and ϵ_{upper} are chosen from a pair of strain gauges and fiber
499 optic cables that are positioned diagonally across the mockup cross-section (e.g., segment 3 and 7, 1 and
500 5, 2 and 6, 4 and 8) at the same longitudinal distances. It is also noted that tension is taken as positive
501 strain values.

502

503 An estimation of bending curvature from LVDT readings is carried out in the following manner. First, the
504 flexural rigidity (EI) of the mockup under three-point bending is calculated from the following equation,
505 which is transformed from the bending deflection formula for the Euler-Bernoulli beam:

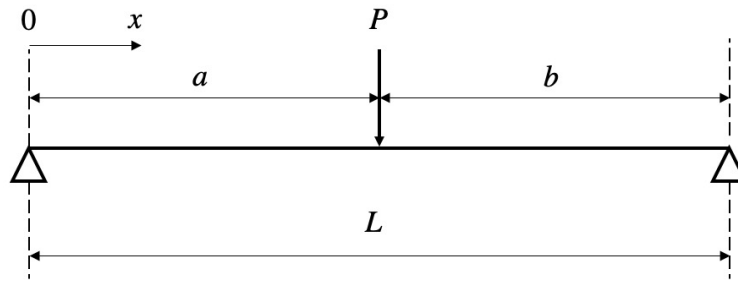
506

$$EI = \begin{cases} (Pbx/6L\delta)(L^2 - b^2 - x^2) & \text{if } 0 \leq x \leq a \\ (Pa(L-x)/6L\delta)(L^2 - a^2 - (L-x)^2) & \text{if } a \leq x \leq L \end{cases} \quad (4)$$

507

508 where P is the vertical point load (obtained from load cell readings); L is the effective length of the
 509 mockup (= 2.92 m); δ is the deflection of the mockup (obtained from LVDT readings); x is the distance
 510 from the left-hand side boundary of the mockup, and a (= 1.44) and b (= 1.53) are the distances from the
 511 left- and right-hand side boundaries of the mockup to the point load, respectively. These parameters are
 512 schematically shown in Figure 14.

513



514

515 Figure 14 Beam model for three-point bending.

516

517 Second, bending moment is calculated from the following equation:

518

$$M = \begin{cases} P(1 - a/L)x & \text{if } 0 \leq x \leq a \\ Pa(x/L - 1) & \text{if } a \leq x \leq L \end{cases} \quad (5)$$

519

520 Finally, bending curvature is calculated from the following equation:

521

$$\kappa = M/EI \quad (6)$$

522

523 Results of the bending curvature estimation are provided in Figure 15 for the different loading directions.

524 The curvature values are reported in m^{-1} , but the unit can be converted into radian/m and degrees/m by a

525 factor of 1.0 and 57.296, respectively. The general trend is that the curvature distributions are triangular

526 with a peak near the middle length of the mockup, which verifies the monitoring results against the
527 theoretical curvature distributions under three-point bending. Also, the curvature values estimated by
528 BOTDA are smaller than those by LUNA and other sensors, which is due to the spatial average nature of
529 the BOTDR/A measurement with a longer gauge length (0.75 m).

530

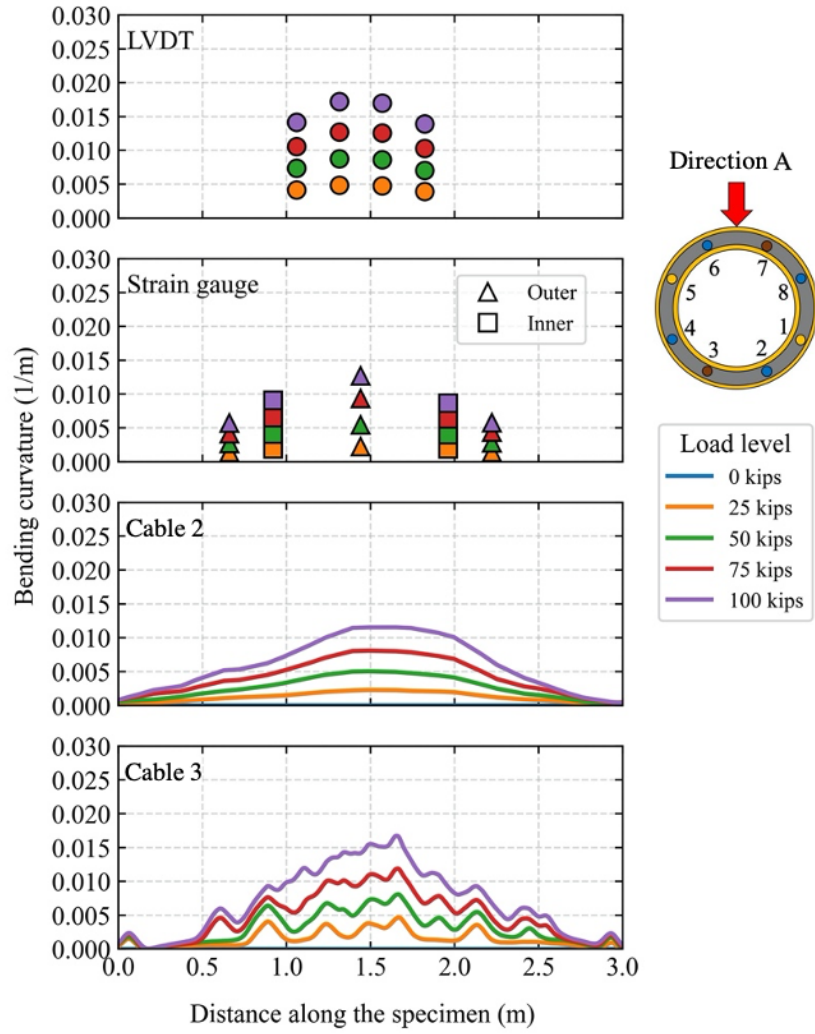
531 Figure 15a shows that relative errors in peak curvature values (near the middle length of the mockup)
532 between Cable 2 and the other sensors at 100 kips are roughly -45% (vs. LVDT), -8% (vs. SG), and -42%
533 (vs. LUNA). Similarly, Figure 15b shows that relative errors for Cable 1, which are calculated to be
534 roughly -36% (vs. LVDT), and -36% (vs. LUNA). This error comparison indicates that Cable 1 has a
535 slightly better curvature monitoring performance than Cable 2, when the mockup deforms elastically in
536 the direction A and B cases. Figure 15c shows a comparison of estimated bending curvature values for the
537 direction C case when the mockup was subjected to plastic deformation. Relative errors in peak curvature
538 values for Cable 2 at 135 kips are approximately -71% (vs. LVDT) and -104% (vs. LUNA), whereas
539 those for Cable 1 are -24% (vs. LVDT) and -48% (vs. LUNA). This comparison reveals that the curvature
540 monitoring performance of Cable 1 is better than that of Cable 2 in the plastic deformation range as well.
541 It is noted that due to malfunction of some strain gauges, peak curvature values could not be obtained
542 from strain gauge readings for the direction B and C cases.

543

544 In summary, Cable 1 provided better bending monitoring performance both in the examined elastic and
545 plastic deformation ranges of the mockup. It should be noted, however, that the mockup deformation was
546 still relatively small in the examined plastic range. Hence, curvature monitoring performance of Cable 1
547 and 2 at a greater plastic deformation range has to be examined carefully in a future study.

548

549



550

551

552

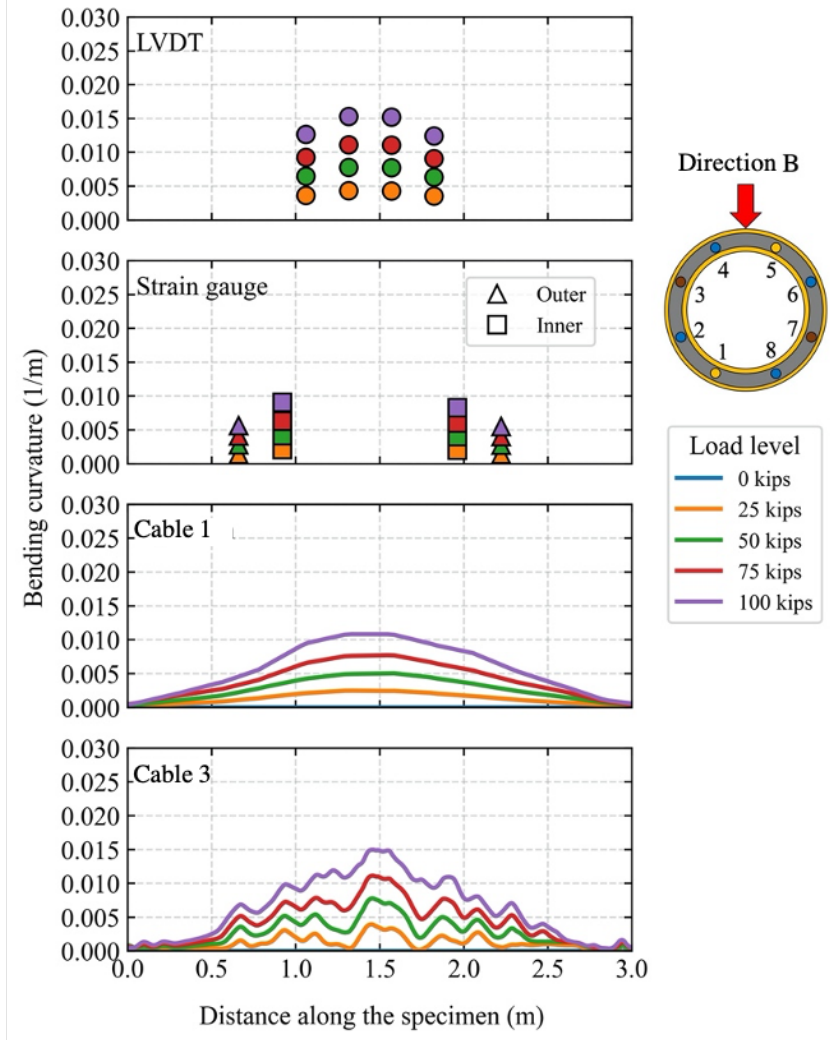
553

554

555

556

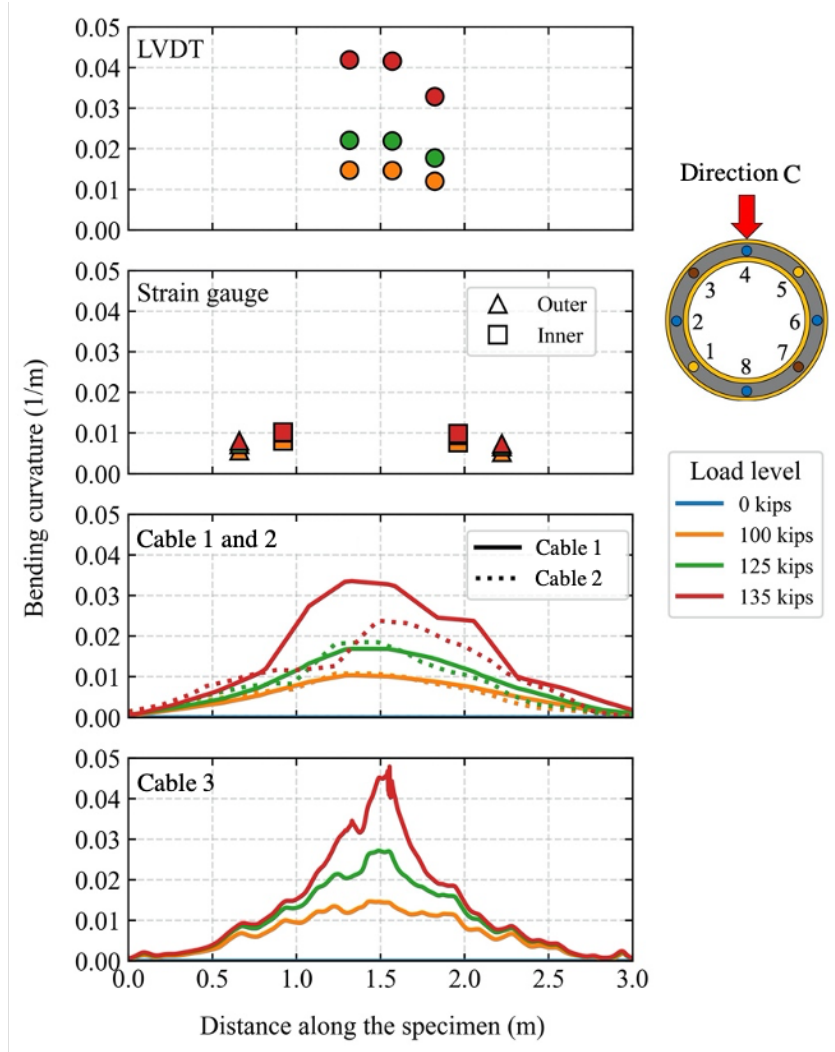
(a)



557

558

(b)



(c)

Figure 15 Bending curvature distributions of the mockup estimated from instrumented sensor readings:

(a) Direction A; (b) Direction B; (c) Direction C.

5.2 Cable performance comparison

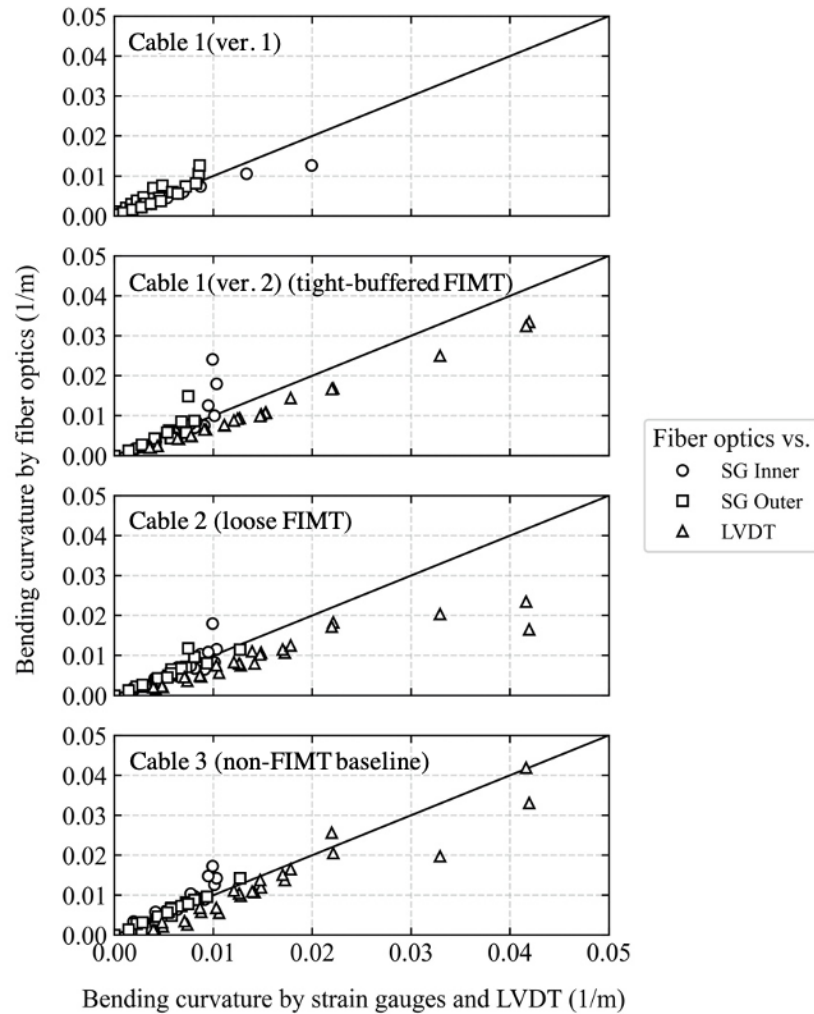
In order to carry out a performance comparison of the fiber optic cables examined in the present experiment, as well as those examined in a previous experiment, simple load vs. strain plots could not be utilized. This is because the bending stiffness of the well mockup in the present and previous experiments

569 is found substantially different from each other; the mockup in the present test is softer than the one in the
570 previous test. Although the steel pipes were made of the same material with the same dimensions in both
571 experiments, and cement slurry was prepared from the identical ingredients with the identical procedure
572 and cured in comparable conditions, small unknown differences during mockup preparation might have
573 changed the bending stiffness of the mockups. Further review is required to identify the cause.

574

575 Consequently, bending curvature (fiber optics) vs. bending curvature (strain gauge and LVDT) plots are
576 prepared for the performance comparison, which is presented in Figure 16. The reference curvature values
577 are calculated from strain gauges and LVDT readings (horizontal axis), whereas curvature values from
578 fiber optic measurements (vertical axis) at the corresponding locations (i.e., the same longitudinal
579 locations as strain gauges and LVDTs) are obtained through linear interpolation of curvature distributions
580 estimated from fiber optic readings.

581



582

583 Figure 16 An evaluation of bending curvature monitoring performance of fiber optic cables against
 584 conventional sensors.

585

586 It is clear that the mockup was stiffer in the previous test, which manifested as the small curvature values
 587 for Cable 1 (version 1). It should be noted that the maximum load was 180 kips in the previous test vs.
 588 135 kips in the present test. Although there are only a couple of data points in the plastic range ($\kappa \sim 0.01$
 589 1/m) for Cable 1 (version 1), its curvature monitoring performance is inferior to that of the other cables
 590 examined in the present experiment, as relative errors are -40% and -25% or less for Cable 1 (version 1)
 591 and the other cables at a reference curvature (x -axis) of 0.02 1/m, respectively.

592

593 The comparison between Cable 1 and 2 corroborates the performance evaluation discussed in earlier
594 sections: Cable 1 is better suited for curvature monitoring than Cable 2 within the bending ranges
595 examined in this study, as the data points for Cable 1 linearly align with the zero-error line, whereas those
596 for Cable 2 are nonlinear at large curvature values ($\kappa > 0.02$ 1/m).

597

598 The deviation of the reference Cable 3 data points from the zero-error line for $0.03 < \kappa < 0.05$ 1/m is due
599 to the spatial local nature of the LUNA measurement. The data points would align better if an averaging
600 method is applied.

601

602 5.3 Comparison with existing research

603

604 It is argued that the results of this study are first-of-their-kind for several reasons. First, the
605 cables used in this study are designed to have high robustness so that they will survive the harsh
606 installation process of tubular in deep offshore wellbore. Existing studies on field applications of
607 distributed strain sensing, in contrast, are limited to onshore wells whose construction processes
608 were well-controlled to allow the use of fragile fiber optic cables (Zhang, Lei, Hashimoto, et al.
609 2020; Lei, Xue, and Hashimoto 2019; Zhang et al. 2019; Sun et al. 2020; Y. Zhang and Xue
610 2019; Sun et al. 2021; 2018). Second, the cables in this study were cemented in the annulus of
611 the mockup without directly attaching them to the inner pipe (i.e., casing). This way of cable
612 installation was performed because it mimics an actual installation process of tubular in an
613 offshore well, which must be simple and efficient enough to comply with the stringent time
614 constraint of the well construction process. In existing research, on the other hand, cables are
615 usually attached directly on tubular by tapes and/or adhesives (Kogure and Okuda 2018; Earles

616 et al. 2010; Pearce, Rambow, et al. 2009; Pearce, Legrand, et al. 2009), which is not feasible in
617 actual field applications. Finally, the abovementioned research does not corroborate their fiber
618 optic strain measurements with data from conventional sensors or analytical solutions. In other
619 words, their fiber optic measurements are qualitative rather than quantitative. For these reasons,
620 it is argued that the contribution of the present study on distributed strain sensing is unique, and
621 it could lead to a step change in the use of distributed strain sensing for the environmental,
622 management, and safety issues of natural gas production.

623

624 **6 Conclusions**

625

626 In this study, distributed strain sensing (DSS) of a well mockup subjected to three-point bending loading
627 was carried out in the laboratory with BOTDR/A and OFDR fiber optic interrogators. The objective of
628 this study was to examine the performance of custom-made fiber optic cables designed specifically for
629 DSS monitoring of an oil and gas well. Key cable characteristics that affect their strain sensing
630 performance were identified. In the experiment, a double pipe well mockup was constructed and fiber
631 optic cables were instrumented in the mockup annulus which was then cemented. Strain gauges and
632 LVDTs were also installed in the mockup to validate distributed fiber optic measurements.

633

634 The following findings are obtained from the analysis of experimental results:

635

- 636 (1) Tight-buffered optical fiber is necessary to achieve sufficient strain sensitivity in distributed strain
637 sensing. Such a fiber optic cable can be manufactured by, for example, (i) encasing fiber in a
638 metal tube (FIMT), (ii) applying the FIMT with a skim-coating polymer layer, and (iii)
639 positioning the FIMT near the center of the cross-section of metal sheath (i.e., the outermost

640 sheath of the fiber optic cable) and filling the gap between the FIMT and metal sheath with
641 polymer.

642 (2) It was demonstrated through laboratory testing that such a cable was capable of measuring both
643 elastic and plastic bending deformations of the well mockup, whereas other cables, which lacked
644 the abovementioned characteristics, failed to capture such deformations with accuracy.

645 (3) As to combined distributed strain and temperature sensing, it was found that the diameter of the
646 gel-filled metal tube, where the optical fibers for the temperature measurement are embedded,
647 would affect the accuracy of the temperature measurement, i.e., the diameter of the gel-filled tube
648 needs to be large enough to isolate the temperature fibers from strains.

649

650 While this research focused on the performance of strain sensing cables in a well mockup under a simple
651 bending load, further research is needed using well mockups under more complex loading and in a real
652 subsurface environment. Future work may include, but not limited to the testing of the fabricated cable in
653 a greater bending deformation range, testing under a combination of axial and bending loads, as well as
654 the validation of the effect of the diameter of DTS FIMT on its strain isolation performance.

655

656

657 **Acknowledgements**

658

659 The authors are grateful for financial support provided by the MH21-S R&D consortium in the Ministry
660 of Economy, Trade and Industry (METI) of the Japanese Government through Japan Oil, Gas and Metals
661 National Corporation (JOGMEC). The authors are also appreciative of technical support provided by the
662 manager and technicians of the 2nd-floor laboratory in Davis Hall (Shakhzod Takhirov, Matthew Cataleta,
663 Llyr Griffith, and Phillip Wong) as well as graduate students and visiting researchers (Peter Hubbard,
664 Hayato Nonaka, and Tianchen Xu) of the University of California, Berkeley. The authors would also like

665 to thank those who are involved in the engineering and fabrication of the fiber optic cables examined in
666 this research, namely, Phillip Morris, Dan Pacheco, and George Farrales from the Prysmian Group, and
667 Karl Zimmermann and Mark Lowell from Lowell Innovation Consulting, LLC.

668

669

670 **References**

671

672 Aydin, G., 2014. Production Modeling in the Oil and Natural Gas Industry: An Application of Trend
673 Analysis. *Petroleum Science and Technology* 32, 555–64.

674 <https://doi.org/10.1080/10916466.2013.825271>.

675 — — —, 2015. Regression Models for Forecasting Global Oil Production. *Petroleum Science and*
676 *Technology* 33, 1822–28. <https://doi.org/10.1080/10916466.2015.1101474>.

677 Aydin, G., Jang, H., Topal, E., 2016. Energy Consumption Modeling Using Artificial Neural Networks:
678 The Case of the World’s Highest Consumers. *Energy Sources, Part B: Economics, Planning and*
679 *Policy* 11, 212–19. <https://doi.org/10.1080/15567249.2015.1075086>.

680 Butler, L.J., Gibbons, N., He, P., Middleton, C., Elshafie, M.Z.E.B., 2016. Evaluating the Early-Age
681 Behaviour of Full-Scale Prestressed Concrete Beams Using Distributed and Discrete Fibre Optic
682 Sensors. *Construction and Building Materials* 126, 894–912.

683 <https://doi.org/10.1016/j.conbuildmat.2016.09.086>.

684 Chen, L., Feng, Y., Okajima, J., Komiya, A., Maruyama, S., 2018. Production Behavior and Numerical
685 Analysis for 2017 Methane Hydrate Extraction Test of Shenhu, South China Sea. *Journal of Natural*
686 *Gas Science and Engineering* 53, 55–66. <https://doi.org/10.1016/j.jngse.2018.02.029>.

687 Cola, S., Bersan, S., Michielin, E., Pangop, F.T., Simonini, P., Schenato, L., Palmieri, L., Bergamo, O.,
688 2019. On Distributed Strains in a CFA Pile via DFOSs Measurements and Numerical Analysis. In

689 *Proceedings of the XVII ECSMGE-2019* <https://www.issmge.org/uploads/publications/51/75/0717->

690 ECSMFE-2019_Cola.pdf.

691 Dale, B.A., Narahara, G.M., Stevens, R.M., 1996. A Case History of Reservoir Subsidence and Wellbore
692 Damage Management in the South Belridge Diatomite Field. In Proceedings of the SPE Western
693 Regional Meeting <https://doi.org/10.2118/35658-ms>.

694 Dou, H., Dong, X., Duan, Z., Ma, Y., Gao, D., 2020. Cement Integrity Loss Due to Interfacial Debonding
695 and Radial Cracking during CO2 Injection. *Energies* 13, 1–17. <https://doi.org/10.3390/en13174589>.

696 Earles, D.M., Stoesz, C.W., Amaral, A.S., Pearce, J.G., Dejongh, H.A., Rambow, F.H.K., 2010. Real-
697 Time Monitoring of Sand Control Completions. In Proceedings of the SPE Annual Technical
698 Conference and Exhibition <https://doi.org/10.2118/134555-ms>.

699 Fabris, C., Schweiger, H.F., Pulko, B., Woschitz, H., Račanský, V., 2021. Numerical Simulation of a
700 Ground Anchor Pullout Test Monitored with Fiber Optic Sensors. *Journal of Geotechnical and*
701 *Geoenvironmental Engineering* 147, 04020163. [https://doi.org/10.1061/\(asce\)gt.1943-](https://doi.org/10.1061/(asce)gt.1943-5606.0002442)
702 [5606.0002442](https://doi.org/10.1061/(asce)gt.1943-5606.0002442).

703 Fredrich, J.T., Arguello, J.G., Deitrick, G.L., Rouffignac, E.P., 2000. Geomechanical Modeling of
704 Reservoir Compaction, Surface Subsidence, and Casing Damage at the Belridge Diatomite Field.
705 *SPE Reservoir Evaluation & Engineering* 3, 8–10. <https://doi.org/10.2118/65354-PA>.

706 Gasda, S.E., Bachu, S., Celia, M.A., 2004. Spatial Characterization of the Location of Potentially Leaky
707 Wells Penetrating a Deep Saline Aquifer in a Mature Sedimentary Basin. *Environmental Geology*
708 46, 707–20. <https://doi.org/10.1007/s00254-004-1073-5>.

709 Gue, C. Y., Wilcock, M., Alhaddad, M. M., Elshafie, M. Z. E. B., Soga, K., Mair, R. J., 2015. The
710 Monitoring of an Existing Cast Iron Tunnel with Distributed Fibre Optic Sensing (DFOS). *Journal*
711 *of Civil Structural Health Monitoring* 5, 573–86. <https://doi.org/10.1007/s13349-015-0109-8>.

712 Hickman, S.H., Hsieh, P.A., Mooney, W.D., Enomoto, C.B., Nelson, P.H., Mayer, L.A., Weber, T.C.,
713 Moran, K., Flemings, P.B., McNutt, M.K., 2012. Scientific Basis for Safely Shutting in the
714 Macondo Well after the April 20, 2010 Deepwater Horizon Blowout. *Proceedings of the National*
715 *Academy of Sciences of the United States of America* 109, 20268–73.

716 <https://doi.org/10.1073/pnas.1115847109>.

717 Inaudi, D., Glisic, B., 2006. Fiber Optic Sensing for Innovative Oil and Gas Production and Transport
718 Systems. *Optical Fiber Sensors* , 4. <https://doi.org/10.1364/OFS.2006.FB3>.

719 Kechavarzi, C., Soga, K., Battista, N. de, Pelecanos, L., Elshafie, M.Z.E.B., Mair, R.J., 2016. *Distributed*
720 *Optical Fibre Sensing for Monitoring Civil Infrastructure - A Practical Guide*.
721 <https://www.icevirtuallibrary.com/isbn/9780727760555>.

722 Klar, A., Bennett, P.J., Soga, K., Mair, R.J., Tester, P., Fernie, R., St John, H.D., Torp-Peterson, G., 2006.
723 Distributed Strain Measurement for Pile Foundations. *Proceedings of the Institution of Civil*
724 *Engineers - Geotechnical Engineering* 159, 135–44. <https://doi.org/10.1680/geng.2006.159.3.135>.

725 Klar, A., Deerberg, G., Janicki, G., Schicks, J., Riedel, M., Fietzek, P., Mosch, T., et al., 2019. Marine
726 Gas Hydrate Technology : State of the Art and Future Possibilities for Europe. *Marine Gas Hydrate*
727 *– an Indigenous Resource of Natural Gas for Europe (MIGRATE)*
728 https://doi.org/10.3289/MIGRATE_WG2.2019.

729 Kogure, T., Okuda, Y., 2018. Monitoring the Vertical Distribution of Rainfall-Induced Strain Changes in
730 a Landslide Measured by Distributed Fiber Optic Sensing With Rayleigh Backscattering.
731 *Geophysical Research Letters* 45, 4033–40. <https://doi.org/10.1029/2018GL077607>.

732 Krietsch, H., Gischig, V., Jalali, M.R., Doetsch, J., Valley, B., Amann, F., 2018. A Comparison of FBG-
733 and Brillouin-Strain Sensing in the Framework of a Decameter-Scale Hydraulic Stimulation
734 Experiment Conference. In *Proceedings of the 52nd US Rock Mechanics / Geomechanics*
735 *Symposium* [https://onepetro.org/ARMAUSRMS/proceedings-abstract/ARMA18/All-](https://onepetro.org/ARMAUSRMS/proceedings-abstract/ARMA18/All-ARMA18/ARMA-2018-800/122534)
736 [ARMA18/ARMA-2018-800/122534](https://onepetro.org/ARMAUSRMS/proceedings-abstract/ARMA18/All-ARMA18/ARMA-2018-800/122534).

737 Lei, X., Xue, Z., Hashimoto, T., 2019. Fiber Optic Sensing for Geomechanical Monitoring: (2)-
738 Distributed Strain Measurements at a Pumping Test and Geomechanical Modeling of Deformation
739 of Reservoir Rocks. *Applied Sciences* 9, 417. <https://doi.org/10.3390/app9030417>.

740 Mayuga, M.N., Allen, D.R., 1969. Subsidence in the Wilmington Oil Field, Long Beach, California,

741 U.S.A. In Proceedings of the Tokyo Symposium on Land Subsidence, International Association of
742 Scientific Hydrology, Studies and Reports in Hydrology, IASH-UNESCO 1,
743 <http://www.saveballona.org/gasoilfields/WilmSubGC.pdf>.

744 McNutt, M.K., Camilli, R., Crone, T.J., Guthrie, G.D., Hsieh, P.A., Ryerson, T.B., Savas, O., Shaffer, F.,
745 2012. Review of Flow Rate Estimates of the Deepwater Horizon Oil Spill. Proceedings of the
746 National Academy of Sciences of the United States of America 109, 20260–67.
747 <https://doi.org/10.1073/pnas.1112139108>.

748 McNutt, M.K., Chu, S., Lubchenco, J., Hunter, T., Dreyfus, G., Murawski, S.A., Kennedy, D.M., 2012.
749 Applications of Science and Engineering to Quantify and Control the Deepwater Horizon Oil Spill.
750 Proceedings of the National Academy of Sciences of the United States of America 109, 20222–28.
751 <https://doi.org/10.1073/pnas.1214389109>.

752 Mohamad, H., Bennet, P.J., Soga, K., Mair, R.J., Bowers, K., 2010. Behaviour of an Old Masonry Tunnel
753 Due to Tunnelling Induced Ground Settlement. *Géotechnique* 60, 927–38.
754 <https://doi.org/10.1680/geot.8.p.074>.

755 Mohamad, H., Soga, K., Amatya, B., 2014. Thermal Strain Sensing of Concrete Piles Using Brillouin
756 Optical Time Domain Reflectometry. *Geotechnical Testing Journal* 37,
757 <https://doi.org/10.1520/GTJ20120176>.

758 Mohamad, H., Soga, K., Bennett, P.J., Mair, R.J., Lim, C.S., 2012. Monitoring Twin Tunnel Interactions
759 Using Distributed Optical Fiber Strain Measurements. *Journal of Geotechnical and*
760 *Geoenvironmental Engineering, ASCE* 138, 957–67. [https://doi.org/10.1061/\(ASCE\)GT.1943-](https://doi.org/10.1061/(ASCE)GT.1943-5606.0000656)
761 [5606.0000656](https://doi.org/10.1061/(ASCE)GT.1943-5606.0000656).

762 Mohamad, H., Soga, K., Pellew, A., Bennett, P.J., 2011. Performance Monitoring of a Secant-Piled Wall
763 Using Distributed Fiber Optic Strain Sensing. *Journal of Geotechnical and Geoenvironmental*
764 *Engineering* 137, 1236–43. [https://doi.org/10.1061/\(asce\)gt.1943-5606.0000543](https://doi.org/10.1061/(asce)gt.1943-5606.0000543).

765 Nagel, N. B., 2001. Compaction and Subsidence Issues within the Petroleum Industry: From Wilmington
766 to Ekofisk and Beyond. *Physics and Chemistry of the Earth, Part A: Solid Earth and Geodesy* 26, 3–

767 14. [https://doi.org/10.1016/S1464-1895\(01\)00015-1](https://doi.org/10.1016/S1464-1895(01)00015-1).

768 Pearce, J.G., Legrand, P., Dominique, T., Childers, B. A., Rambow, F.H.K., Dria, D. E., 2009. Real-Time
769 Compaction Monitoring with Fiber-Optic Distributed Strain Sensing (DSS). In Proceedings of the
770 SPWLA 50th Annual Logging Symposium [https://www.onepetro.org/conference-paper/SPWLA-](https://www.onepetro.org/conference-paper/SPWLA-2009-85310)
771 2009-85310.

772 Pearce, J.G., Rambow, F.H.K., Shroyer, W., Huckabee, P., Jongh, H. de, Dria, D. E., Childers, B. A.,
773 Hall, T. S., Dominique, T., 2009. High Resolution, Real-Time Casing Strain Imaging for Reservoir
774 and Well Integrity Monitoring: Demonstration of Monitoring Capability in a Field Installation. In
775 Proceedings of the 2009 SPE Annual Technical Conference and Exhibition
776 <https://doi.org/10.2118/124932-ms>.

777 Pelecanos, L., Soga, K., Chung, M.P.M., Ouyang, Y., Kwan, V., 2017. Distributed Fibre-Optic
778 Monitoring of an Osterberg-Cell Pile Test in London. *Géotechnique Letters* 7, 1–9.
779 <https://doi.org/10.1680/jgele.16.00081>.

780 Pelecanos, L., Soga, K., Elshafie, M.Z. E. B., Battista, N. de, Kechavarzi, C., Gue, C. Y., Ouyang, Y.,
781 Seo, H.-J., 2018. Distributed Fiber Optic Sensing of Axially Loaded Bored Piles. *Journal of*
782 *Geotechnical and Geoenvironmental Engineering* 144, 1–16.
783 [https://doi.org/10.1061/\(ASCE\)GT.1943-5606.0001843](https://doi.org/10.1061/(ASCE)GT.1943-5606.0001843).

784 Rabaiotti, C., Hauswirth, D., Fischli, F., Facchini, M., Puzrin, A., 2017. Structural Health Monitoring of
785 Airfield Pavements Using Distributed Fiber-Optics Sensing. In Proceedings of the 4th Conf. on
786 Smart Monitoring, Assessment and Rehabilitation of Civil Structures (SMAR 2017)
787 https://data.smar-conferences.org/SMAR_2017_Proceedings/papers/133.pdf.

788 Roberts, D, 1953. Shear Prevention in the Wilmington Field. [https://www.onepetro.org/conference-](https://www.onepetro.org/conference-paper/API-53-146)
789 [paper/API-53-146](https://www.onepetro.org/conference-paper/API-53-146).

790 Sasaki, T., 2019. Fibre Optic Monitoring and Finite Element Analysis of Well Integrity in Methane
791 Hydrate Reservoirs. <https://doi.org/10.17863/CAM.41244>.

792 Sasaki, T., Park, J., Soga, K., Momoki, T., Kawaguchi, K., Muramatsu, H., Imasato, Y., Balagopal, A.,

793 Fontenot, J., Hall, T., 2019. Distributed Fibre Optic Strain Sensing of an Axially Deformed Well
794 Model in the Laboratory. *Journal of Natural Gas Science and Engineering*
795 <https://doi.org/10.1016/j.jngse.2019.103028>.

796 Schwall, G. M., Denney, C. A., 1994. Subsidence Induced Casing Deformation Mechanisms in the Ekofisk
797 Field. In *Proceedings of the 1994 Eurock SPE/ISRM Rock Mechanics in Petroleum Engineering*
798 Conference <https://doi.org/10.2118/28091-MS>.

799 Soga, K., Luo, L., 2018. Distributed Fiber Optics Sensors for Civil Engineering Infrastructure Sensing.
800 *Journal of Structural Integrity and Maintenance* 3, 1–21.
801 <https://doi.org/10.1080/24705314.2018.1426138>.

802 Sun, Y., Xue, Z., Hashimoto, T., Lei, X., Zhang, Y., 2020. Distributed Fiber Optic Sensing System for
803 Well-Based Monitoring Water Injection Tests—A Geomechanical Responses Perspective. *Water*
804 *Resources Research* 56, <https://doi.org/10.1029/2019WR024794>.

805 Sun, Y., Xue, Z., Hashimoto, T., Zhang, Y., 2021. Optically Quantifying Spatiotemporal Responses of
806 Water Injection-Induced Strain via Downhole Distributed Fiber Optics Sensing. *Fuel* 283, 118948.
807 <https://doi.org/10.1016/j.fuel.2020.118948>.

808 Sun, Y., Xue, Z., Zhang, Y., Hashimoto, T., Park, H., 2018. Field Measurements Using Distributed Fiber-
809 Optic Sensing Technology and Numerical Simulation of Geomechanical Deformation Caused by
810 CO₂ Injection. In *Proceedings of the 14th International Conference on Greenhouse Gas Control*
811 *Technologies, GHGT-14* https://papers.ssrn.com/sol3/papers.cfm?abstract_id=3365651.

812 Teodoriu, C., Yuan, Z., Schubert, J., Amani, M., 2012. Experimental Measurements of Mechanical
813 Parameters of Class G Cement. In *Proceedings of the SPE/EAGE European Unconventional*
814 *Resources Conference and Exhibition* <https://doi.org/10.2118/153007-MS>.

815 Wu, Q., 2019. Advanced Distributed Fiber Optic Sensors for Monitoring Real-Time Cementing
816 Operations and Long Term Zonal Isolation. <https://repositories.lib.utexas.edu/handle/2152/77392>.

817 Yamamoto, K., 2015. Overview and Introduction: Pressure Core-Sampling and Analyses in the 2012-

818 2013 MH21 Offshore Test of Gas Production from Methane Hydrates in the Eastern Nankai Trough.
819 Marine and Petroleum Geology 66, 296–309. <https://doi.org/10.1016/j.marpetgeo.2015.02.024>.

820 Yamamoto, K., Dallimore, S.R., 2008. Aurora-JOGMEC-NRCan Mallik 2006-2008 Gas Hydrate
821 Research Project Progress. Fire in the Ice Summer, 1–5.
822 <https://netl.doe.gov/sites/default/files/publication/HMNewsSummer08.pdf>.

823 Yamamoto, K., Kanno, T., Wang, X.-X., Tamaki, M., Fujii, T., Chee, S.-S., Wang, X.-W., Pimenov, V.,
824 Shako, V., 2017. Thermal Responses of a Gas Hydrate-Bearing Sediment to a Depressurization
825 Operation. RSC Advances 7, 5554–77. <https://doi.org/10.1039/C6RA26487E>.

826 Yamamoto, K., Terao, Y., Fujii, T., Ikawa, T., Seki, M., Matsuzawa, M., Kanno, T., 2014. Operational
827 Overview of the First Offshore Production Test of Methane Hydrates in the Eastern Nankai Trough.
828 In Proceedings of the Offshore Technology Conference <https://doi.org/10.4043/25243-MS>.

829 Yoneda, J., Masui, A., Konno, Y., Jin, Y., Egawa, K., Kida, M., Ito, T., Nagao, J., Tenma, N., 2015.
830 Mechanical Properties of Hydrate-Bearing Turbidite Reservoir in the First Gas Production Test Site
831 of the Eastern Nankai Trough. Marine and Petroleum Geology 66, 471–86.
832 <https://doi.org/10.1016/j.marpetgeo.2015.02.029>.

833 Yudovich, A., Chin, L.V., Morgan, D.R., 1988. Casing Deformation in Ekofisk. In Proceedings of the
834 Offshore Technology Conference <https://doi.org/10.4043/5623-ms>.

835 Zhang, C.C., Shi, B., Gu, K., Liu, S.P., Wu, J.H., Zhang, S., Zhang, L., Jiang, H.T., Wei, G.Q., 2018.
836 Vertically Distributed Sensing of Deformation Using Fiber Optic Sensing. Geophysical Research
837 Letters 45, 11,732-11,741. <https://doi.org/10.1029/2018GL080428>.

838 Zhang, S., Liu, H., Cheng, J., DeJong, M.J., 2020. A Mechanical Model to Interpret Distributed Fiber
839 Optic Strain Measurement at Displacement Discontinuities. Structural Health Monitoring
840 <https://doi.org/10.1177/1475921720964183>.

841 Zhang, S., Liu, H., Coulibaly, A.A.S., DeJong, M.J., 2020. Fiber Optic Sensing of Concrete Cracking and
842 Rebar Deformation Using Several Types of Cable. Structural Control and Health Monitoring 1–23.
843 <https://doi.org/10.1002/stc.2664>.

844 Zhang, Y., Lei, X., Hashimoto, T., Xue, Z., 2020. In Situ Hydromechanical Responses during Well
845 Drilling Recorded by Fiber-Optic Distributed Strain Sensing. *Solid Earth* 11, 2487–97.
846 <https://doi.org/10.5194/se-11-2487-2020>.

847 Zhang, Y., Xue, Z., 2019. Deformation-Based Monitoring of Water Migration in Rocks Using Distributed
848 Fiber Optic Strain Sensing: A Laboratory Study. *Water Resources Research* 55, 8368–83.
849 <https://doi.org/10.1029/2019WR024795>.

850 Zhang, Y., Xue, Z., Park, H., Shi, J.-Q., Kiyama, T., Lei, X., Sun, Y., Liang, Y., 2019. Tracking CO₂
851 Plumes in Clay-Rich Rock by Distributed Fiber Optic Strain Sensing (DFOSS): A Laboratory
852 Demonstration. *Water Resources Research* 55, 856–67. <https://doi.org/10.1029/2018WR023415>.
853